

1 **Parameterization of Size of Organic and Secondary Inorganic Aerosol for** 2 **Efficient Representation of Global Aerosol Optical Properties**

3 Haihui Zhu^{1*}, Randall V. Martin^{1,2}, Betty Croft^{2,1}, Shixian Zhai³, Chi Li¹, Liam Bindle¹, Jeffrey
4 R. Pierce⁴, Rachel Y.-W. Chang², Bruce E. Anderson⁵, Luke D. Ziemba⁵, Johnathan W. Hair⁵,
5 Richard A. Ferrare⁵, Chris A. Hostetler⁵, Inderjeet Singh¹, Deepangsu Chatterjee¹, Jose L.
6 Jimenez⁶, Pedro Campuzano-Jost⁶, Benjamin A. Nault⁷, Jack E. Dibb⁸, Joshua S. Schwarz⁹,
7 Andrew Weinheimer¹⁰

8 ¹ Department of Energy, Environmental & Chemical Engineering, Washington University in St. Louis, St. Louis, MO,
9 USA

10 ² Department of Physics and Atmospheric Science, Dalhousie University, Halifax, Nova Scotia, Canada

11 ³ Harvard John A. Paulson School of Engineering and Applied Sciences, Harvard University, Cambridge, MA, USA

12 ⁴ Department of Atmospheric Science, Colorado State University, Fort Collins, CO, USA

13 ⁵ NASA Langley Research Center, Hampton, VA, USA

14 ⁶ Cooperative Institute for Research in Environmental Sciences and Department of Chemistry, University of Colorado,
15 Boulder, CO, USA

16 ⁷ Center for Aerosol and Cloud Chemistry, Aerodyne Research, Inc., Billerica, MA, USA

17 ⁸ Institute for the Study of Earth, Oceans, and Space, University of New Hampshire, Durham, NH, USA

18 ⁹ National Oceanic and Atmospheric Administration Chemical Sciences Laboratory, Boulder, CO, USA

19 ¹⁰ National Center for Atmospheric Research, Boulder, CO, USA

20 *Correspondence:* Haihui Zhu (haihuizhu@wustl.edu)

21 **Abstract** Accurate representation of aerosol optical properties is essential for modeling and remote sensing of
22 atmospheric aerosols. Although aerosol optical properties are strongly dependent upon the aerosol size distribution,
23 use of detailed aerosol microphysics schemes in global atmospheric models is inhibited by associated computational
24 demands. Computationally efficient parameterizations for aerosol size are needed. In this study, airborne
25 measurements over the United States (DISCOVER-AQ) and South Korea (KORUS-AQ) are interpreted with a global
26 chemical transport model (GEOS-Chem) to investigate the variation in aerosol size when organic matter (OM) and
27 sulfate-nitrate-ammonium (SNA) are the dominant aerosol components. The airborne measurements exhibit a strong
28 correlation ($r = 0.83$) between dry aerosol size and the sum of OM and SNA mass concentration (M_{SNAOM}). A global
29 microphysical simulation (GEOS-Chem-TOMAS) indicates that M_{SNAOM} , and the ratio between the two components
30 ($\frac{OM}{SNA}$) are the major indicators for SNA and OM dry aerosol size. A parameterization of dry effective radius (R_{eff}) for
31 SNA and OM aerosol is designed to represent the airborne measurements ($R^2 = 0.74$, slope = 1.00) and the GEOS-
32 Chem-TOMAS simulation ($R^2 = 0.72$, slope = 0.81). When applied in the GEOS-Chem high-performance model, this
33 parameterization improves the agreement between the simulated aerosol optical depth (AOD) and the ground-

34 measured AOD from the Aerosol Robotic Network (AERONET; R^2 from 0.68 to 0.73, slope from 0.75 to 0.96). Thus,
35 this parameterization offers a computationally efficient method to represent aerosol size dynamically.

36 **1 Introduction**

37 Aerosol size has numerous effects on aerosol physical and chemical properties and further on atmospheric chemistry.
38 Aerosol size-dependent heterogeneous chemistry affects gaseous oxidants that in turn affect production rates of
39 aerosol components such as sulfate and secondary organic aerosol (Ervens et al., 2011; Estillore et al., 2016). Aerosol
40 size also affects loss rates due to dry and wet deposition (Seinfeld and Pandis, 2016). Both direct and indirect aerosol
41 radiative forcing are sensitive to aerosol size, as aerosol size affects the interaction between particles and radiation,
42 and the rate at which a particle grows to a cloud droplet (Adams and Seinfeld, 2002; Faxvog and Roessler, 1978;
43 Mishchenko et al., 2002; Emerson et al., 2020). The size dependence of aerosol extinction and scattering phase
44 function also affects the retrieval of aerosol properties from satellites (Levy et al., 2013; Kahn et al., 2005; Jin et al.,
45 2023). Aerosol size affects the fraction of particles that deposit in the body when breathing as well as location within
46 the body where they deposit (Hinds and Zhu, 1999). An appropriate representation of aerosol size is essential for
47 modeling aerosol composition and optical properties (Kodros and Pierce, 2017), interpreting satellite data (Levy et al.,
48 2013; Kahn et al., 2005), studying climate processes (Twomey, 2007; Kellogg, 1980), and moving from aerosol
49 exposure towards dose in health studies (Kodros et al., 2018).

50 The evolution of the aerosol size distribution is affected by various processes, such as nucleation, condensation,
51 coagulation, and deposition. Nucleation events contribute to the number of particles in the nucleation mode (diameters
52 less than about 10 nm) and thus tend to decrease the mean aerosol size for a population (Aalto et al., 2001). In polluted
53 areas with high emission rates of aerosol precursors, mean aerosol size tends to increase by condensation and
54 coagulation (Sakamoto et al., 2016; Sun et al., 2011). Dry and wet aerosol deposition have strong size dependencies
55 due to competing physical processes (Emerson et al., 2020; Ruijrok et al., 1995; Reutter et al., 2009). The aerosol size
56 distribution can be simulated using aerosol microphysical schemes, such as the Two Moment Aerosol Sectional
57 (TOMAS; Adams and Seinfeld, 2002) microphysics model, the Advanced Particle Microphysics (APM; Yu and Luo,
58 2009) model, the Global Model of Aerosol Processes (GLOMAP; Mann et al., 2010), and the Modal Aerosol Module
59 (MAM4; Liu et al., 2016). These schemes have valuable prognostic capabilities; however, their computational cost
60 has limited their use in Chemistry Climate Models (CCMs) or Chemical Transport Models (CTMs). For example, the
61 wall clock time increases by about 2.5 times when APM is enabled in GEOS-Chem CTM relative to the bulk model
62 (GCST et al., 2023). Only 3 of the 10 models that included aerosols, studied by the Atmospheric Chemistry and
63 Climate Model Intercomparison Project, include online size-resolved aerosol microphysics, reflecting its
64 computational cost and complexity (Lamarque et al., 2013; Liu et al., 2012; Szopa et al., 2013; Kodros and Pierce,
65 2017).

66 Methods are needed to better represent aerosol size in CCMs or CTMs without a microphysics scheme (referred to as
67 bulk models). These bulk models usually use prescribed relationships to obtain size-resolved aerosol properties (Croft
68 et al., 2005; Karydis et al., 2011; Zhai et al., 2021), which may insufficiently represent the temporal and spatial

69 variation (Kodros and Pierce, 2017). For example, in the GEOS-Chem CTM, a fixed dry aerosol geometric mean
70 radius (R_g) is assumed for organic matter (OM) and sulfate-nitrate-ammonium (SNA), which is based on analysis of
71 long-term aerosol composition and scattering measurements provided by the IMPROVE network across the
72 continental U.S. (Latimer and Martin, 2019). However, subsequent analysis by Zhai *et al.* (2021) found that this
73 aerosol size underestimated the aerosol mass scattering efficiency and the aerosol extinction coefficients during an
74 aircraft campaign over South Korea (KORUS-AQ). Thus, neglect of aerosol microphysical processes that shape
75 aerosol size distributions can be a significant source of uncertainty in aerosol optical properties in a CTM. A balance
76 between computational cost and representativeness of aerosol size is needed. One option is to use models with size-
77 resolved aerosol microphysics models to inform bulk models, such as was done for the parameterization of biomass
78 burning aerosol size by Sakamoto *et al.* (2016).

79 Recent airborne measurements offer information to evaluate and improve the simulation of aerosol size. DISCOVER-
80 AQ (Deriving Information on Surface Conditions from Column and Vertically Resolved Observations Relevant to Air
81 Quality) was a multi-year campaign over four U.S. cities that provides 3-D resolved measurements of atmospheric
82 gas composition, aerosol composition, size distribution, and optical properties (Choi *et al.*, 2020; Sawamura *et al.*,
83 2017; Chu *et al.*, 2015). KORUS-AQ (the Korea-United States Air Quality Study) offers similar measurements in a
84 different environment with higher aerosol mass loadings (Choi *et al.*, 2020; Zhai *et al.*, 2021; Nault *et al.*, 2018; Jordan
85 *et al.*, 2020).

86 To study the global variation in aerosol size, we explore airborne measurements from DISCOVER-AQ and KORUS-
87 AQ, as well as output from the GEOS-Chem-TOMAS microphysics model. We focus on OM and SNA, which
88 dominate fine aerosol composition in populated areas (Weagle *et al.*, 2018; Geng *et al.*, 2017; Meng *et al.*, 2019; Van
89 Donkelaar *et al.*, 2019; Li *et al.*, 2017). The driving factors for variation in aerosol size are examined. A
90 parameterization of aerosol size using these driving factors is proposed. This parameterization is then applied to a
91 GEOS-Chem high-performance model bulk simulation for global aerosol optical depth (AOD), which is evaluated by
92 ground-measured AOD from the Aerosol Robotic Network (AERONET).

93 **2 Observations and Models**

94 **2.1 Observations**

95 **2.1.1 Aircraft measurements**

96 We examine airborne measurements from two NASA campaigns, DISCOVER-AQ and KORUS-AQ. DISCOVER-
97 AQ includes four deployments in Maryland (MD), California (CA), Texas (TX), and Colorado (CO). KORUS-AQ is
98 an international cooperative field study program conducted in South Korea (KO), sponsored by NASA and the South
99 Korean government through the National Institute of Environmental Research. The year as well as the date and altitude
100 ranges of each deployment are in Table 1.

101

102 **Table 1. Temporal and spatial coverage of each aircraft deployment**

Campaign	Year	Date Range	Altitude from surface
MD	2011	07/01-07/29	0 to 5 km
TX	2013	09/04-09/29	0 to 5 km
CA	2013	01/16-02/06	0 to 4 km
CO	2014	07/17-08/10	0 to 6 km
KO	2016	05/02-06/11	0 to 8 km

103

104 Measurements used in this study include aerosol composition, ambient aerosol extinction, aerosol number size
 105 distribution, gas tracer species, and meteorological data. Measurement methods are listed in Table 2. Measured aerosol
 106 mass is converted from standard to ambient condition before analysis using ambient temperature and pressure. We
 107 use OM directly measured during KORUS-AQ. We use water soluble organic carbon (OC) and a parameterized ratio
 108 between OM and OC (Philip et al., 2014) to calculate OM for DISCOVER-AQ. The parameterized OM is evaluated
 109 with KORUS-AQ data, and overall consistency is found (Figure A1; Appendix A). For both campaigns, dust
 110 concentration is derived from Ca^{2+} and Na^+ assuming non-sea salt Ca^{2+} accounts for 7.1% of dust mass (Shah et al.,
 111 2020):

$$Dust = \frac{([Ca^{2+}] - 0.0439 \frac{[Na^+]}{2})}{0.071} \quad \text{Eqn. (1)}$$

112 Sea salt is calculated from measured Na^+ following previous studies (Remoundaki et al., 2013; Malm et al., 1994;
 113 Snider et al., 2016). The crustal component is removed by subtracting 10 % of $[Al^{3+}]$ (Remoundaki et al., 2013). A
 114 2.54 scalar is applied to $[Na^+]_{ss}$ to account for $[Cl^-]$ (Malm et al., 1994):

$$Sea\ Salt = 2.54([Na^+] - 0.1[Al^{3+}]) \quad \text{Eqn. (2)}$$

115 Effective radius (R_{eff}) (Hansen and Travis, 1974), defined as the area-weighted mean radius of a particle population,
 116 is used as a surrogate for aerosol size:

$$R_{eff} = \frac{\int r \pi r^2 n(r) dr}{\int \pi r^2 n(r) dr} \quad \text{Eqn. (3)}$$

117 Measurement data are screened for dust influence by excluding data with the sum of SNA and OM ($M_{SNAOM} < 4 \times$
 118 dust mass.

119 **Table 2. Aircraft observations used in this study***

Variables	DISCOVER-AQ	KORUS-AQ
Bulk aerosol ionic composition	IC-PILS ^a	SAGA ^b
Sub-micron non-refractory aerosol composition	TOC-PILS ^c	HR-ToF-AMS ^d
Refractory black carbon concentration		SP2 ^e
Dry aerosol size distribution	UHSAS ^f or LAS ^g	LAS ^g
Aerosol extinction profile at 532 nm		HSRL ^h
NO ₂	4-Channel Chemiluminescence Instrument ⁱ	
Relative humidity (RH)		DLH ^j

120 * Adapted from Zhai et al. (2021)

121 ^a Ion Chromatography Particle-Into-Liquid Sampler, with a 1.3 μm inlet cutoff aerodynamic diameter (Lee et al., 2003;
122 Hayes et al., 2013).

123 ^b Soluble Acidic Gases and Aerosol (SAGA) instrument (Dibb et al., 2003). The cutoff aerodynamic diameter of the
124 inlet is around 4 μm (McNaughton et al., 2007).

125 ^c Water-soluble organic carbon Particle-Into-Liquid Sampler, with a 1 μm inlet cutoff diameter at 1 atmosphere
126 ambient pressure (Sullivan et al., 2019; Timonen et al., 2010).

127 ^d University of Colorado Boulder High-Resolution Time-of-Flight Aerosol Mass Spectrometer (HR-ToF-AMS) with
128 a 1 μm inlet cutoff diameter (Nault et al., 2018; Guo et al., 2021; Canagaratna et al., 2007).

129 ^e Single-Particle Soot Photometer (SP2), measuring refractory black carbon with a volume equivalent diameter of 100-
130 500 nm (Lamb et al., 2018; Schwarz et al., 2006).

131 ^f Particles with mobility diameters between 60 to 1000 nm can be measured by Ultra-High Sensitivity Aerosol
132 Spectrometer (UHSAS), which illuminates particles with a laser and relate the single-particle light scattering intensity
133 and count rate measured over a wide range of angles to the size-dependent particle concentration (Moore et al., 2021).
134 Particles in the sample are dried to less than 20 % RH.

135 ^g Particles between 100 to 5000 nm measured by Laser Aerosol Spectrometer (LAS, TSI model 3340). The principle
136 of LAS is the same as that of UHSAS, but with a different laser wavelength (1054 nm for the UHSAS and 633 nm for
137 the LAS) and intensity (about 100 times higher for the UHSAS). These differences affect how the instrument sizes
138 non-spherical or absorbing aerosols (Moore et al., 2021). Particles in the sample are dried to less than 20 % RH.

139 ^h NASA Langley airborne High Spectral Resolution Lidar (HSRL) (Hair et al., 2008).

140 ⁱ National Center for Atmospheric Research (NCAR) 4-Channel Chemiluminescence Instrument (Weinheimer et al.,
141 1993)

142 ^j NASA Diode Laser Hygrometer (DLH) (Podolske et al., 2003).

143 **2.1.2 AERONET AOD**

144 We use ground-based AOD observations to evaluate our parameterization and simulated AOD. The Aerosol Robotic
145 Network (AERONET) is a worldwide network that provides long-term sun photometer measured AOD, and is
146 conventionally considered as the ground truth for evaluating model-simulated (Zhai et al., 2021; Meng et al., 2021;
147 Jin et al., 2023) or satellite-retrieved AOD (Levy et al., 2013; Wang et al., 2014a; Kahn et al., 2005; Lyapustin et al.,
148 2018). We use the Version 3 Level 2 database, which includes an improved cloud screening algorithm (Giles et al.,
149 2019). AOD at 550 nm wavelength, interpolated based on the local Ångström exponent at 440 and 670 nm channels,
150 is used in this study. For each site, we use data for the year 2017, excluding months with less than 20 days of
151 measurements and excluding sites with less than 4 months of observations.

152 **2.2 GEOS-Chem simulation**

153 We interpret the aircraft observations with the GEOS-Chem chemical transport model (www.geos-chem.org, last
154 access: 30 October 2022). GEOS-Chem is driven by offline meteorological data from the Goddard Earth Observing
155 System (GEOS) of the NASA Global Modeling and Assimilation Office (Schubert et al., 1993). We use the high-
156 performance implementation of GEOS-Chem (GCHP) (Eastham et al., 2018; Bindle et al., 2021) to examine the
157 effect of variation in aerosol size on AOD. We also use the TOMAS microphysical scheme, coupled with the standard
158 GEOS-Chem implementation (GEOS-Chem Classic), to explicitly resolve aerosol microphysics. The bulk and the
159 microphysics simulations share common emissions and chemical mechanisms. They are both conducted for the year
160 2017 and driven by MERRA-2 meteorological fields.

161 The GEOS-Chem aerosol simulation includes the sulfate-nitrate-ammonium system (Fountoukis and Nenes, 2007;
162 Park, 2004), primary and secondary carbonaceous aerosols (Park et al., 2003; Wang et al., 2014b; Marais et al., 2016;
163 Pye et al., 2010), sea salt (Jaeglé et al., 2011), and mineral dust (Fairlie et al., 2007). The primary emission data are
164 from the Community Emissions Data System (CEDS_{GBD-MAPS}; McDuffie et al., 2020). Dust emission inventories
165 include updated natural dust emission (Meng et al., 2021b), and anthropogenic fugitive, combustion, and industrial
166 dust (AFCID; Philip et al., 2017). Resolution-dependent soil NO_x, sea salt, biogenic VOC, and natural dust emissions
167 are calculated offline at native meteorological resolution to produce consistent emissions across resolution (Weng et
168 al., 2020; Meng et al., 2021b). Biomass burning emissions use the Global Fire Emissions Database, version 4 (GFED4)
169 (Van Der Werf et al., 2017). We estimate organic matter (OM) from primary organic carbon using the same OM/OC
170 parameterizations as applied for DISCOVER-AQ (Philip et al., 2014; Canagaratna et al., 2015). Dry and wet
171 deposition follows Amos *et al.* (2012), with a standard resistance-in-series dry deposition scheme (Wang et al., 1998).
172 Wet deposition includes scavenging processes from convection and large-scale precipitation (Liu et al., 2001).

173 Global relative humidity dependent aerosol optical properties are based on the Global Aerosol Data Set (GADS)
174 (Kopke P., 1997; Martin et al., 2003) with updates for SNA and OM (Latimer and Martin, 2019), mineral dust (Zhang
175 et al., 2013), and absorbing brown carbon (Hammer et al., 2016). In the current GEOS-Chem model, the SNA and

176 OM R_{eff} of particular interest here are based on co-located measurements of aerosol scatter and mass from the
177 IMPROVE network at U.S. national parks over the period 2000-2010, together with a κ -Kohler framework for aerosol
178 hygroscopicity (Kreidenweis et al., 2008) as implemented by Latimer and Martin (2019). Aerosol extinction is
179 calculated as the sum of extinction from each aerosol component with aerosol optical properties listed in Table A1, as
180 described in Appendix A2.

181 A global GCHP simulation (Eastham et al., 2018) version 13.0.0 (DOI: 10.5281/zenodo.4618180) that includes
182 advances in performance and usability (Martin et al., 2022), is conducted on a C90 cubed-sphere grid corresponding
183 to a horizontal resolution of about 100 km, with a spin-up time of 1 month.

184 The TOMAS microphysics scheme, coupled with the GEOS-Chem simulation, conserves aerosol mass, and tracks
185 particles with diameters from approximately 1 nm to 10 μm (Adams and Seinfeld, 2002). Microphysical processes in
186 TOMAS include nucleation, condensation, evaporation, coagulation, and wet and dry deposition (Adams and Seinfeld,
187 2002). Nucleation in TOMAS follows a ternary scheme (sulfuric acid, ammonia, and water) when ammonia mixing
188 ratios are greater than 0.1 ppt; otherwise, a binary nucleation scheme is used (Napari et al., 2002). The nucleation rate
189 is scaled by 10^{-5} to better match the observations (Westervelt et al., 2013). The condensation and evaporation algorithm
190 is based on a study from Tzivion *et al.* (1989), including interaction with secondary organic aerosol (D'Andrea et al.,
191 2013). Interstitial coagulation in clouds is also included (Pierce et al., 2015).

192 For each size bin, TOMAS tracks the mass and number of sulfate, sea salt, black carbon, OC, dust, and water. Primary
193 sulfate emissions have 2 lognormal modes: 15% of the mass with a number median diameter (NMD) of 10 nm and
194 geometric standard deviation (σ) of 1.6 and the remainder with a NMD of 70 nm and σ of 2 (Adams and Seinfeld,
195 2003). The size of emitted carbonaceous particles varies depending on the source: those produced by fossil fuel have
196 a NMD of 30 nm and σ of 2, while biofuel and biomass burning particles are emitted with a NMD of 100 nm and σ
197 of 2 (Pierce et al., 2007). Meteorology and most of the emissions in GEOS-Chem-TOMAS follow the bulk simulation,
198 except that online schemes are used for dust (Zender et al., 2003) and sea salt (Jaeglé *et al.* 2011).

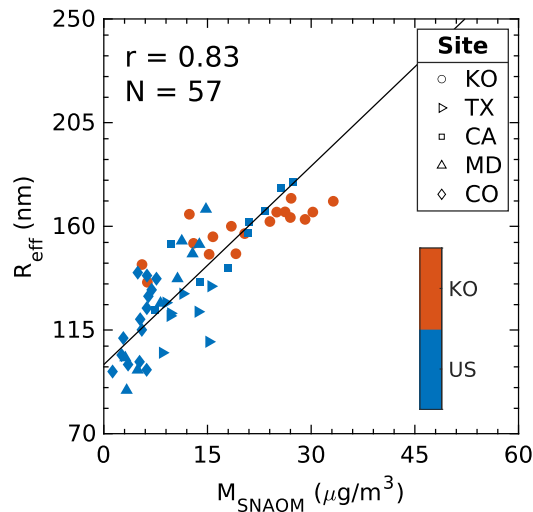
199 The GEOS-Chem-TOMAS (version 13.2.1. DOI: 10.5281/zenodo.5500717) is used to provide insights into global
200 scale aerosol size variation and the driving factors. For computational feasibility, a one-year global simulation is
201 conducted with a horizontal resolution of $4^\circ \times 5^\circ$ and 47 vertical layers from surface to 0.01 hPa. The spin-up time is
202 1 month. Aerosols are tracked in 15 size bins with particle diameters ranging from about 3 nm to 10 μm . We also
203 conducted a $2^\circ \times 2.5^\circ$ simulation for October to evaluate the sensitivity of our conclusions to the resolution of the
204 aerosol microphysics simulation.

205 **3 Development of a Parameterization of Aerosol Size**

206 We first examine the aircraft measurements for insight into the observed variation in aerosol size. Then we apply the
207 size-resolved GEOS-Chem-TOMAS model to extend our analysis to the global scale and identify driving factors of
208 aerosol size. We subsequently develop and test a parameterization of aerosol size for use in bulk models.

209 **3.1 Observed variation in aerosol size**

210 Figure 1 shows the daily-mean dry effective radius from DISCOVER-AQ and KORUS-AQ as a function of aerosol
211 mass. Aerosol size, in terms of dry R_{eff} , ranges from 90 nm to 179 nm for DISCOVER-AQ, which is generally smaller
212 than for KORUS-AQ that ranges from 135 nm to 174 nm. M_{SNAOM} from DISCOVER-AQ ($1.4 \mu\text{g}/\text{m}^3$ to $27.4 \mu\text{g}/\text{m}^3$)
213 is also generally less than that from KORUS-AQ ($5.5 \mu\text{g}/\text{m}^3$ to $33.2 \mu\text{g}/\text{m}^3$). A strong correlation ($r = 0.83$) between
214 aerosol size and M_{SNAOM} is evident. R_{eff} from KORUS-AQ is less sensitive to M_{SNAOM} (slope = 1.23) compared to
215 DISCOVER-AQ (slope = 3.57). The relatively large particle size at low mass concentration during KORUS-AQ might
216 reflect the influence of aged aerosol transported from upwind (Jordan et al., 2020; Zhai et al., 2021; Nault et al., 2018).

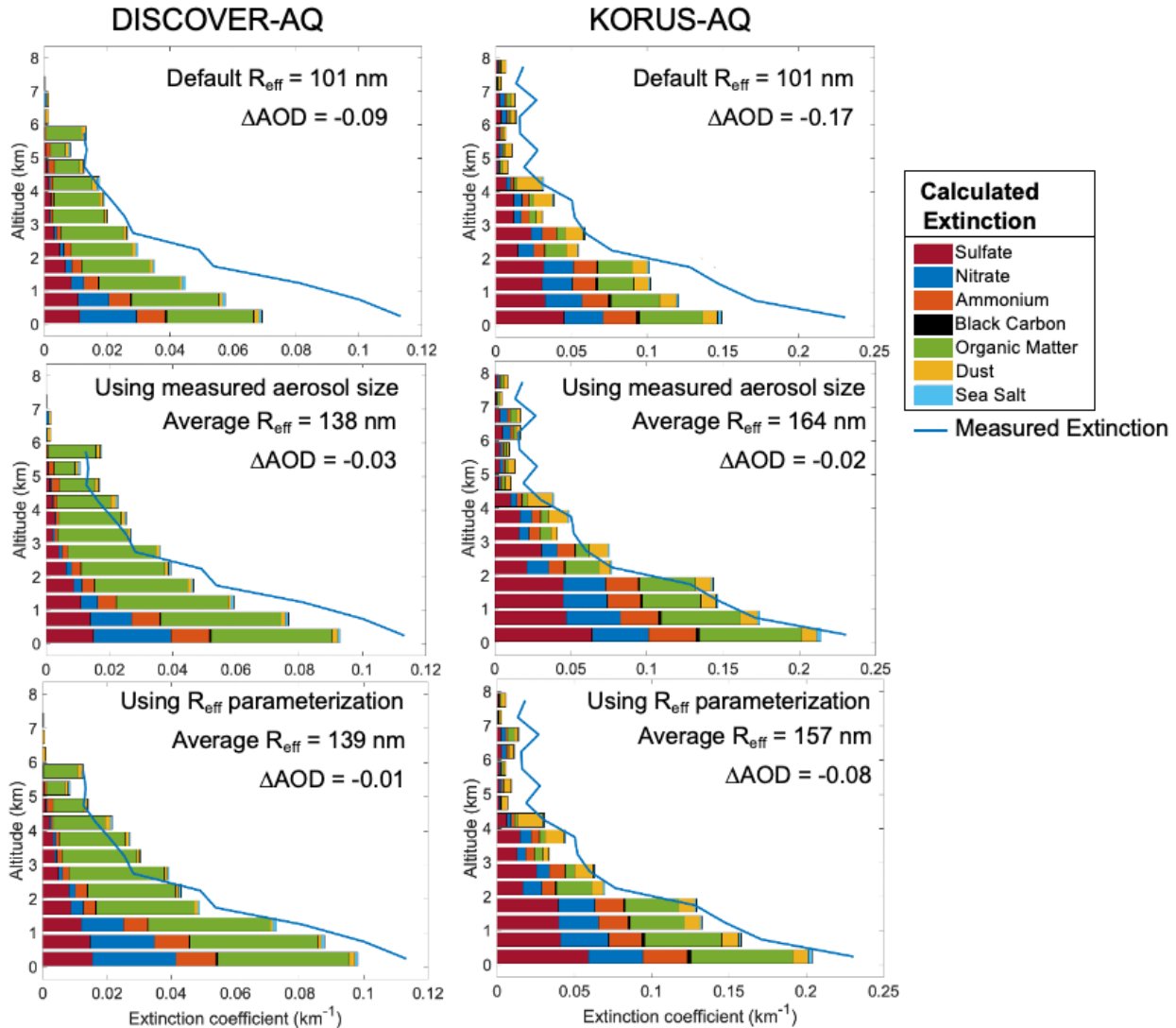


217

218 **Figure 1. Airborne measurements of dry effective radius (R_{eff}) versus the sum of SNA and OM mass**
219 **(M_{SNAOM}) for DISCOVER-AQ (Maryland is abbreviated as MD, California as CA, Texas as TX, Colorado as**
220 **CO) and for KORUS-AQ (KO) campaigns. Each point represents a daily average for the entire flight profile.**
221 **Only data with $M_{\text{SNAOM}} > 4 \times \text{Dust mass}$ is used.**

222 The positive relationship between dry aerosol size and mass of SNA and OM reflects the roles of emission,
223 condensation, and coagulation in simultaneously increasing aerosol size and mass. This general tendency is also
224 observed by many other studies (e.g., Sakamoto et al., 2016; Rodríguez et al., 2007; Sun et al., 2012; Bahreini et al.,
225 2003) despite variable aerosol sources and growth mechanisms. In cities, the joint increases in aerosol size and mass
226 are usually attributable to anthropogenic emissions and condensation (Tian et al., 2019; Sun et al., 2011; Huang et al.,
227 2013). In remote areas, biomass burning shifts the particle size distribution toward larger radii due to high emission
228 rates and coagulation in plumes (Rissler et al., 2006; Ramnarine et al., 2019) that, for example, increase both aerosol
229 size and mass from the wet season to the dry season in Amazonia (Rissler et al., 2006; Andreae et al., 2015). The
230 positive relationship between aerosol size and mass suggests the possibility of using aerosol mass as a predictor of
231 R_{eff} .

232 We examine the ability of the GEOS-Chem bulk model to reproduce the observed extinction. The top panel of Figure
233 2 compares the measured aerosol extinction profiles to calculated aerosol extinction profiles using default R_{eff} . Details
234 about the calculation are described in Appendix A2. Both measured and calculated extinction profiles exhibit
235 increasing extinction toward the surface associated with increasing aerosol mass concentrations. However, biases are
236 apparent for both DISCOVER-AQ and KORUS-AQ. The R_{eff} from KORUS-AQ shown in Figure 1 have a mean value
237 of 164 nm, larger than the value of 101 nm inferred by Latimer & Martin (2019) based on measurements of aerosol
238 scatter and mass by the U.S. IMPROVE network. This bias was previously noted by Zhai *et al.* (2021). The mean R_{eff}
239 from DISCOVER-AQ of 138 nm is also larger than the inferred value. This likely reflects representativeness
240 differences since the DISCOVER-AQ deployments focused on major urban areas during months of high aerosol
241 loadings, while the IMPROVE measurements were at national parks throughout the year. The middle panel shows the
242 calculated extinction using the measured aerosol size distribution. Applying the measured aerosol size distribution
243 addresses most discrepancies between the calculated and measured aerosol extinction profile for both KORUS-AQ
244 and DISCOVER-AQ. The corresponding discrepancies in AOD estimation also significantly decreased (from 0.09 to
245 0.03 for DISCOVER-AQ and from 0.17 to 0.02 for KORUS-AQ). The reduced discrepancies support the conclusions
246 from Zhai *et al.* (2021) that the GEOS-Chem aerosol size is underestimated for KORUS-AQ and motivate
247 parameterization of R_{eff} for efficient representation of aerosol size for global scale aerosol modeling.



248

249 **Figure 2. Aerosol extinction profile for the DISCOVER-AQ and KORUS-AQ aircraft campaigns. Blue lines**
 250 **are the measured extinction profiles. Horizontal bars are calculated extinction using (top) default GEOS-**
 251 **Chem R_{eff} , (middle) measured R_{eff} , and (bottom) parameterized R_{eff} (described in Section 3.3), together with**
 252 **measured aerosol composition and RH. The aerosol extinction calculation is described in Appendix A.**

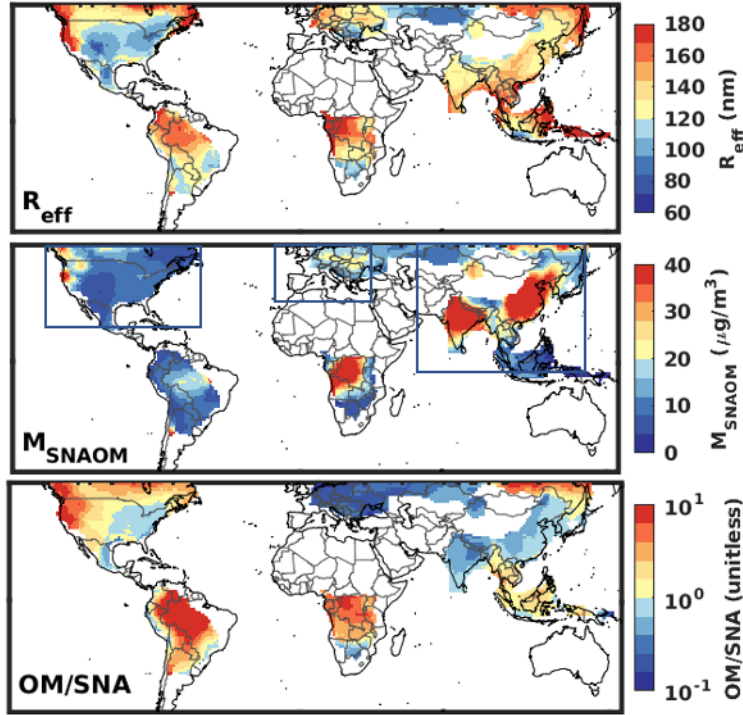
253 3.2 Driving factors

254 Given the strong positive correlation of aerosol mass with aerosol size, we further examine this relationship globally
 255 using GEOS-Chem coupled with the TOMAS aerosol microphysics scheme. To focus on areas that are dominated by
 256 SNA and OM, we only include grid boxes with $M_{\text{SNAOM}} > 90\%$ of the aerosol mass. Inspection of the GEOS-Chem-
 257 TOMAS size distribution across continental regimes reveals a general tendency for the distribution to shift toward
 258 smaller sizes as R_{eff} decreases and toward larger sizes as R_{eff} increases, thus supporting the use of the single summary
 259 statistic of R_{eff} for aerosol size. The top panel of Figure 3 shows the geographic distribution of annual mean surface
 260 layer dry R_{eff} for grid boxes that meet the criterion. Among the areas of interest, biomass burning regions of Central

261 Africa, South America, and boreal forests of North America exhibit the highest surface R_{eff} of about 180 nm. Industrial
262 areas such as East Asia and South Asia also exhibit high R_{eff} of about 130 nm, given an abundance of particle emissions
263 and gaseous precursors. The lowest surface R_{eff} of about 80 nm is found in North America, where aerosol mass
264 concentrations are low.

265 The middle panel of Figure 3 shows the simulated M_{SNAOM} from GEOS-Chem-TOMAS. Enhanced M_{SNAOM}
266 concentrations of over $40 \mu\text{g}/\text{m}^3$ are apparent over East Asia and South Asia, reflecting intense anthropogenic
267 emissions. Another M_{SNAOM} hotspot can be seen in Central Africa, driven by biomass burning during the dry season
268 (Van Der Werf et al., 2017; McDuffie et al., 2021) and sometimes exacerbated by anthropogenic emissions (Ngo et
269 al., 2019). Moving from North America to Europe, and then to Asia (defined by boxes in the middle panel), M_{SNAOM}
270 concentrations exhibit a generally increasing tendency (mean value of 11, 17, and $25 \mu\text{g}/\text{m}^3$, respectively), consistent
271 with the R_{eff} tendency (mean value of 124, 133, and 136 nm, respectively) in the top panel and aligning with the
272 relationship between aircraft measurements over the U.S. and South Korea.

273 However, in South America, where R_{eff} is among the highest, M_{SNAOM} is relatively low. This discrepancy motivates
274 the search for other factors, such as aerosol composition, that are associated with aerosol size. In South America,
275 aerosol mass is mostly from natural sources, particularly biomass burning during the dry seasons. R_g for a particle
276 population from biomass burning ranges from 60 nm to 170 nm (Rissler et al., 2006; Reid et al., 2005; Janhäll et al.,
277 2010), usually larger than that of primary sulfate aerosol (5 to 35 nm) (Whitey, 1978; Plaza et al., 2011). Therefore,
278 the relative abundance of OM in the total M_{SNAOM} can serve as another predictor of R_{eff} . The bottom panel of Figure
279 3 shows the ratio between OM and SNA mass. In addition to the Amazon basin, the biomass burning regions of Central
280 Africa and boreal forests in Asia and North America are all areas with high OM mass fractions, which contribute to
281 their high R_{eff} .



282

283 **Figure 3: Geographic distribution of GEOS-Chem-TOMAS-simulated annual mean surface layer aerosol**
 284 **properties; (top) R_{eff} when $M_{SNAOM} > 90\%$ of aerosol mass, (middle) the sum of SNA and OM mass (M_{SNAOM}),**
 285 **and (bottom) OM/SNA.**

286 3.3 Parameterization and evaluation

287 We use Multiple Linear Regression (MLR) to derive a parameterization of dry R_{eff} for SNA and OM as a function of
 288 M_{SNAOM} and OM/SNA. We sample the GEOS-Chem-TOMAS simulation for locations dominated by M_{SNAOM} ($> 90\%$).
 289 We include all qualified data (8,569 grid boxes) from the planetary boundary layer (PBL) to focus on this region,
 290 while randomly sample 0.5% of simulations in the free troposphere (217,772 grid boxes) to allow the influence of
 291 remote regions in the training set. The reason for focusing on the PBL is twofold. First, the PBL generally has the
 292 highest aerosol loading that largely determines the columnar mass and AOD (Koffi et al., 2016; Zhai et al., 2021; Tian
 293 et al., 2019). Second, the PBL is the domain where most model-measurement difference exists (Figure 2, top panel).

294 Taking the logarithm of R_{eff} and the logarithm of the two predictors facilitates linear relationships for regression,
 295 which yields the initial parameterization

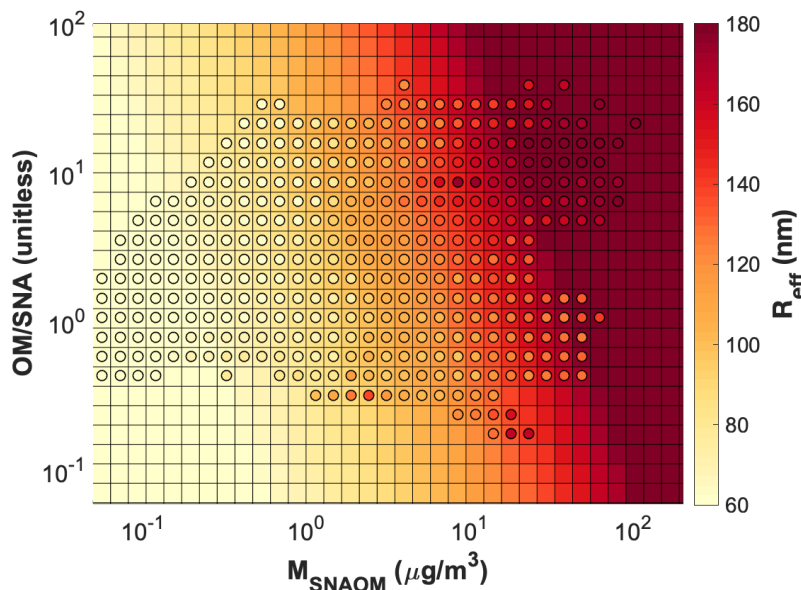
$$R_{eff} = 78.3 M_{SNAOM}^{0.20} \left(\frac{OM}{SNA} \right)^{0.065} \quad \text{Eqn. (4)}$$

296 where R_{eff} has units of nm, M_{SNAOM} has units of $\mu\text{g}/\text{m}^3$, and OM/SNA is unitless. The R_{eff} parameterization is driven
 297 primarily by the mass of SNA and OM, modulated by the ratio of OM to SNA. This equation well represents the
 298 variation of R_{eff} during the aircraft campaigns with an R^2 of 0.74 (Figure B1, top left). The slope below unity (0.90)

299 likely reflects the effect of coarse model resolution, which dilutes the particle or precursor concentration in turn
300 reducing condensation and coagulation growth (AboEl-Fetouh et al., 2022; Ramnarine et al., 2019; Sakamoto et al.,
301 2016). Adjustment to this parameterization to account for these effects and align the slope with the airborne
302 measurements rather than the model results in a final parameterization of

$$R_{eff} = 87.0 M_{SNAOM}^{0.20} \left(\frac{OM}{SNA} \right)^{0.065} \quad \text{Eqn. (5)}$$

303 Figure 4 shows the distribution of dry R_{eff} based on GEOS-Chem-TOMAS and Eqn. (5). Circles in Figure 4 show the
304 mean values of the sampled GEOS-Chem-TOMAS simulated R_{eff} as a function of simulated M_{SNAOM} concentrations,
305 ranging from 0.02 to 102 $\mu\text{g}/\text{m}^3$, and OM/SNA ranging from 0.13 to 55. Simulated R_{eff} extends from 15 nm when both
306 M_{SNAOM} and OM/SNA are low (0.09 $\mu\text{g}/\text{m}^3$ and 1.3, respectively), up to 282 nm when M_{SNAOM} and OM/SNA are high
307 (about 44 $\mu\text{g}/\text{m}^3$ and 14 respectively). The background color indicates our parameterized R_{eff} . A high degree of
308 consistency exists between the parameterized R_{eff} and simulated R_{eff} , especially in the free troposphere where large
309 gradients in R_{eff} exist, with overall for the troposphere an R^2 of 0.72, and a slope of 0.81 (Figure B1, bottom right). At
310 the lower end of R_{eff} , the agreement between simulation and the parameterization can also be found in Figure B1,
311 which shows that the small R_{eff} are reproduced by the parameterization. Despite the overall consistency, a few
312 differences exist. When aerosol mass concentration is high, the parameterization tends to yield a higher R_{eff} than in
313 the GEOS-Chem-TOMAS simulation, since the adjustment using aircraft measurements led to 11% increase in R_{eff} .
314 At M_{SNAOM} near 10 $\mu\text{g}/\text{m}^3$ and OM/SNA near 10, the simulation indicates higher R_{eff} than the parameterization,
315 reflecting dilution downwind of biomass burning that reduces the aerosol mass concentration but has less influence
316 on particle size in GEOS-Chem-TOMAS (Park et al., 2013; Rissler et al., 2006; Sakamoto et al., 2016). A 10-20%
317 underestimation in the parameterization at low OM/SNA reflects the advection and dilution downwind of urban areas
318 and in the free troposphere (Yue et al., 2010; Asmi et al., 2011). Evaluation of our parameterization versus the GEOS-
319 Chem-TOMAS simulation of $2^\circ \times 2.5^\circ$ for October yields similar results but explains an additional 14% of the variance
320 in simulated R_{eff} , providing additional evidence of the fidelity of the parameterization.



321

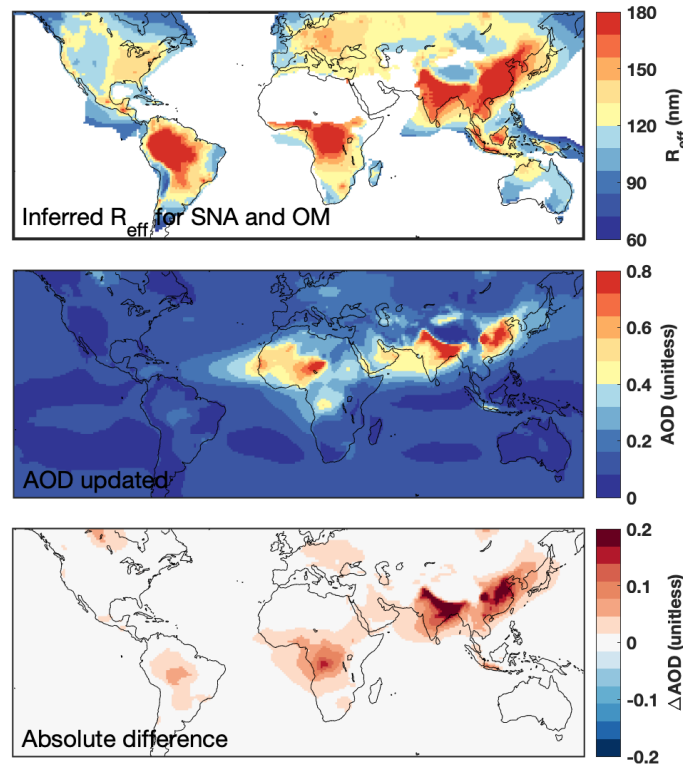
322 **Figure 4. Dry R_{eff} as a function of M_{SNAOM} and OM/SNA when SNA and OM are dominant (>90%). Each**
 323 **circle represents the mean value of the GEOS-Chem-TOMAS simulated R_{eff} in each bin. Background color**
 324 **indicates the parameterized R_{eff} .**

325 When applied to the airborne measurements, this parameterization only slightly overestimates the measured R_{eff} from
 326 DISCOVER-AQ (139 nm vs. 138 nm) and slightly underestimates R_{eff} from KORUS-AQ (157 nm vs. 164 nm).
 327 Discrepancies between calculated and measured extinction from aircraft campaigns are largely reduced (Figure 2,
 328 bottom panel) with AOD biases of 0.01 and 0.08 for DISCOVER-AQ and KORUS-AQ, respectively. Minor
 329 differences are still present in aerosol extinction above 4 km for KORUS-AQ, but a physical explanation remains
 330 elusive since the calculated extinction is biased even if measured aerosol size and composition are used; instrument
 331 uncertainties may play a role. Nonetheless, effects on columnar AOD from these disagreements aloft are minor (<5%).

332 We then apply Eqn. (5) to a GEOS-Chem bulk simulation to calculate R_{eff} and AOD. The top panel of Figure 5 shows
 333 the annual mean dry R_{eff} for surface SNA and OM aerosol. The parameterized R_{eff} is usually higher than the default
 334 value of about 100 nm in GEOS-Chem over land, and lower than that over the ocean, with a normalized root mean
 335 square deviation (NRMSD) of 43.8%. The parameterized R_{eff} is the highest in biomass burning regions in South
 336 America and Central Africa, as well as industrial regions in Asia, similar to the pattern found in the GEOS-Chem-
 337 TOMAS simulation. The parameterized R_{eff} and its horizontal variation diminish with altitude (Figure B2), with the
 338 mean R_{eff} of 85 nm at the surface decreasing by 18.8% to 69 nm at about 5 km. By design, the parameterization has
 339 little effect in regions and seasons where and when M_{SNAOM} is not dominant, since the parameterization only affects
 340 R_{eff} of SNA and OM.

341 The middle panel of Figure 5 shows the simulated AOD, with the corresponding difference between the base
 342 simulation and the updated simulation in the bottom panel. To accommodate the parameterized R_{eff} , a look-up table
 343 with a wide range of R_{eff} (0.02 μm to 1.7 μm) and the corresponding extinction efficiencies for OM and SNA is created

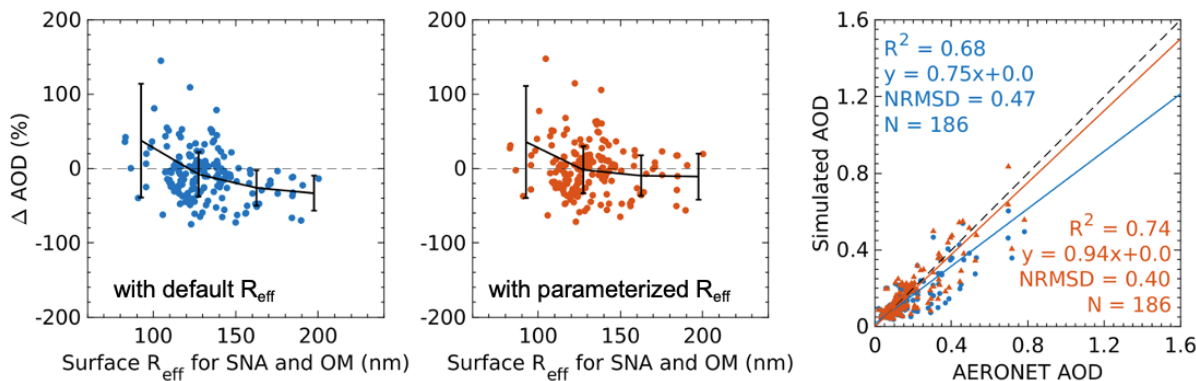
344 based on Mie Theory (Mishchenko et al., 2002, 1999). This update generally increases aerosol mass scattering by
 345 increasing the mass extinction efficiency, in turn, increasing AOD over regions with strong anthropogenic sources,
 346 such as East Asia (by 0.10, 28.3%) and South Asia (by 0.14, 31.1%). It also slightly increases AOD over regions
 347 influenced by wildfires, such as South America (by 0.02, 19.7%), Central Africa (by 0.03, 22.7%), and the boreal
 348 forests in Europe (by 0.01, 9.9%). Most increases occur near the surface (Figure B3), where the highest aerosol mass
 349 loading and mass extinction efficiency exist. The NRMSD between original and updated GEOS-Chem simulated AOD
 350 is 18.9% globally, and 25.6% over continents.



351
 352 **Figure 5. (Top) Surface dry R_{eff} for SNA and OM calculated using Eqn. (5) and GEOS-Chem bulk model**
 353 **simulated SNA and OM mass. R_{eff} is shown when M_{SNAOM} is greater than 80% of the total aerosol mass.**
 354 **(Middle) The GEOS-Chem simulated AOD using inferred R_{eff} . (Bottom) the absolute difference between**
 355 **updated AOD and default AOD using dry $R_{eff} = 101$ nm.**

356 Although R_{eff} is only one of many processes affecting AOD, we evaluate the effect of the parameterization on the
 357 GEOS-Chem simulation of AOD to assess its implications. The left and middle panels of Figure 6 show the
 358 discrepancy between GEOS-Chem simulated AOD and AERONET AOD as a function of the parameterized surface
 359 R_{eff} for SNA and OM. The simulation using the default R_{eff} (Figure 6, left panel) slightly overestimates AOD at sites
 360 with small parameterized R_{eff} and underestimates AOD at sites with large parameterized R_{eff} . The overestimates occur
 361 primarily in western Europe where SNA and OM concentrations are low, while the underestimates happen mainly
 362 over industrial regions in East Asia, Southeast Asia, and biomass burning areas in South America and Central Africa,

363 where the SNA and OM mass loading are high (Figure B4). The underestimates are mitigated when applying the
 364 parameterized R_{eff} in GEOS-Chem (Figure 6, middle panel), yielding increased consistency between the measured
 365 (AERONET) AOD and simulated AOD (Figure 6, right; R^2 change from 0.68 to 0.74, slope from 0.75 to 0.94).



366
 367 **Figure 6. (Left and middle) Percent increase in GEOS-Chem simulated AOD minus AERONET AOD as a**
 368 **function of parameterized surface dry R_{eff} for SNA and OM. Black lines represent the mean values of ΔAOD**
 369 **in each 35 nm bin; error bars represent the corresponding standard deviation. (Right) Scatter plot of**
 370 **AERONET versus simulated AOD with the default R_{eff} (blue dots, line, and text), and with the parameterized**
 371 **R_{eff} (red dots, line, and text). The 1:1 line is dashed. NRMSD is the normalized root mean square deviation**
 372 **between the two datasets. N is the number of points in each dataset.**

373 4 Conclusion

374 Aerosol size strongly determines mass scattering efficiency with implications for calculation of aerosol optical
 375 properties. Prior work found that the global mean dry aerosol size used in a bulk aerosol model induced low bias
 376 versus measured extinction in a region with a high aerosol loading (Zhai et al., 2021). We interpreted aircraft
 377 measurements from DISCOVER-AQ and KORUS-AQ with a chemical transport model (GEOS-Chem) to better
 378 understand regional variation in aerosol size. The measurements had a strong positive correlation ($r = 0.83$) between
 379 aerosol size and mass of sulfate-nitrate-ammonium (SNA) and organic matter (OM), reflecting the high condensation
 380 and coagulation rates where emissions of particles and the gaseous precursors are abundant, indicating the possibility
 381 of using aerosol mass as a predictor of aerosol size.

382 To gain a broader perspective of the global variation in aerosol size, we used the TOMAS microphysics package of
 383 the GEOS-Chem model to simulate the monthly mean aerosol mass, composition, and size distribution. We used
 384 effective radius (R_{eff}) as a surrogate of aerosol size and examined its relationship with aerosol mass and components
 385 where SNA and OM were dominant. We found that the sum of SNA and OM concentration, and the ratio between
 386 them, were the major predictors of R_{eff} . We used GEOS-Chem-TOMAS model output to derive a parameterization of
 387 R_{eff} , which well reproduced R_{eff} measured from the aircraft campaigns ($R^2 = 0.74$). When applied in the bulk GEOS-
 388 Chem high-performance model, the parameterization tended to increase R_{eff} of SNA and OM over regions with high
 389 concentrations of SNA and OM, and decrease R_{eff} elsewhere relative to the standard model. This led to a global

390 normalized root mean square deviation (NRMSD) of 43.8% between the original and updated surface R_{eff} . The
391 parameterized R_{eff} tended to increase the vertical gradient in extinction relative to the standard model, due to the
392 decrease in R_{eff} with altitude. The NRMSD of global mean AOD between the original and updated simulations was
393 18.9%, with the most significant regional AOD increase of 0.14 in South Asia, where aerosol mass loadings are high.
394 This parameterization led to improved consistency of GEOS-Chem simulated AOD with AERONET AOD (R^2 from
395 0.68 to 0.74; slope from 0.75 to 0.94), by increasing AOD at high R_{eff} .

396 Overall, the simple parameterization of R_{eff} derived in this study improved the accuracy in modeling aerosol optical
397 properties without imposing additional computational expense. Other chemical transport models and modeling of
398 other size-related processes, such as heterogeneous chemistry, photolysis frequencies, and dry deposition, may also
399 benefit from the parameterized R_{eff} . Future work could include additional parameters to better summarize the aerosol
400 size distribution. Further developments in computational efficiency of aerosol microphysics models and more
401 abundant measurements of aerosol size and optical properties would both offer opportunities for further advances.

402

403 *Data availability.* AERONET data can be found at <https://aeronet.gsfc.nasa.gov/>. Aircraft data during DISCOVER-
404 AQ are available at <https://asdc.larc.nasa.gov/project/DISCOVER-AQ>. KORUS-AQ data can be found at
405 <https://doi.org/10.5067/Suborbital/KORUSAQ/DATA01>.

406 *Author contributions.* HZ and RVM designed the study. HZ performed the data analysis and model simulations with
407 contributions from BC, SZ, CL, LB, JRP, IS, DC, and RYWC. BEA, LDZ, JWH, RAF, CAH, JLJ, PCJ, JED, JSS,
408 AW, and BAN contributed to KORUS-AQ and DISCOVER-AQ campaign measurements. HZ and RVM wrote the
409 paper with input from all authors.

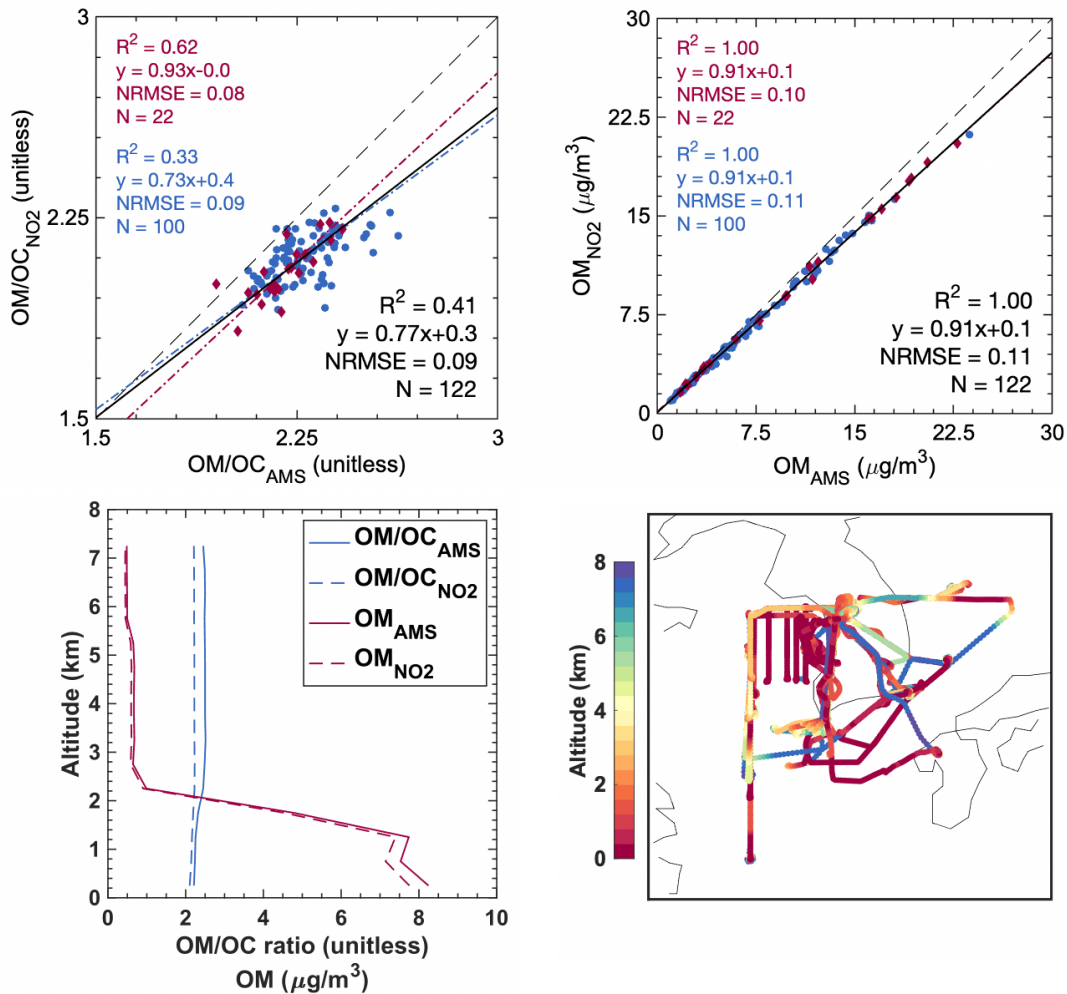
410 *Competing interests.* The contact author has declared that neither they nor their co-authors have any competing
411 interests.

412 *Financial support.* This work was supported by NASA Grant 80NSSC21K1343. JRP was funded by the US NSF
413 Atmospheric Chemistry program, under grant AGS-1950327. JLJ and PCJ were supported by NASA Grant
414 80NSSC21K1451 and NNX15AT96G. BAN was supported by NASA Grant 80NSSC22K0283. JED was supported
415 by NASA Grant NNX15AT88G.

416 **Appendix A**

417 **A1 Application of spatially and temporally varying OM/OC ratio**

418 The top panel of Figure A1 shows scatter plots of the estimated and measured OM/OC and OM during the KORUS-
 419 AQ campaign. The estimation is obtained by applying to OC measurement a NO₂ inferred OM/OC from (Philip *et al.*,
 420 2014), with a subsequent correction factor of 1.09 suggested by Canagaratna *et al.* (2015). Estimated OM is compared
 421 with measured OM by AMS during the campaign. Overall consistency is evident between NO₂-derived OM/OC and
 422 measured OM/OC. The agreement is better below 500 m than above (left panel, R² = 0.62 vs. 0.33). The discrepancy
 423 at high altitudes is mainly due to the low NO₂ (<0.2 ppbv), where the Philip *et al.* (2014) equation is not applicable.
 424 An average OM/OC ratio (2.1) is applied in this case. A high degree of consistency exists between the estimated OM
 425 and measured OM, with R² = 0.99 and slope = 0.91 for data from all altitudes (right panel), thus supporting the use of
 426 estimated OM in our analyses. The bottom left panel compares the vertical profile of the estimates and measurements,
 427 yielding overall consistency.



428

429 **Figure A1. Scatter plots of estimated and measured OM/OC (top left) and OM (top right) during KORUS-**
430 **AQ. Each point represents a mean value of AMS measurement for a 1-hour interval. Red diamonds, lines,**
431 **and texts represent data from 0-500 m altitude. Blue dots, lines, and text represent data above 500 m from the**
432 **ground. Black solid lines and texts represent the line of best fit for all the data. The 1:1 line is dashed.**
433 **NRMSD is the normalized root mean square deviation between the two datasets. N is the number of points in**
434 **each dataset. (Bottom left) Mean values of OM/OC and OM from measurements and estimations along the**
435 **altitude. (Bottom right) Flight tracks during KORUS-AQ.**

436

437 **A2 Aerosol Extinction Calculation in GEOS-Chem**

438 Extinction (Ext) of radiation by aerosols is represented as the sum of extinction due to each of the aerosol components
 439 using the following equation:

$$Ext_k = \frac{3Q_{ext,k}M_k}{4\rho_k R_{eff,k}} \quad \text{Eqn. (3)}$$

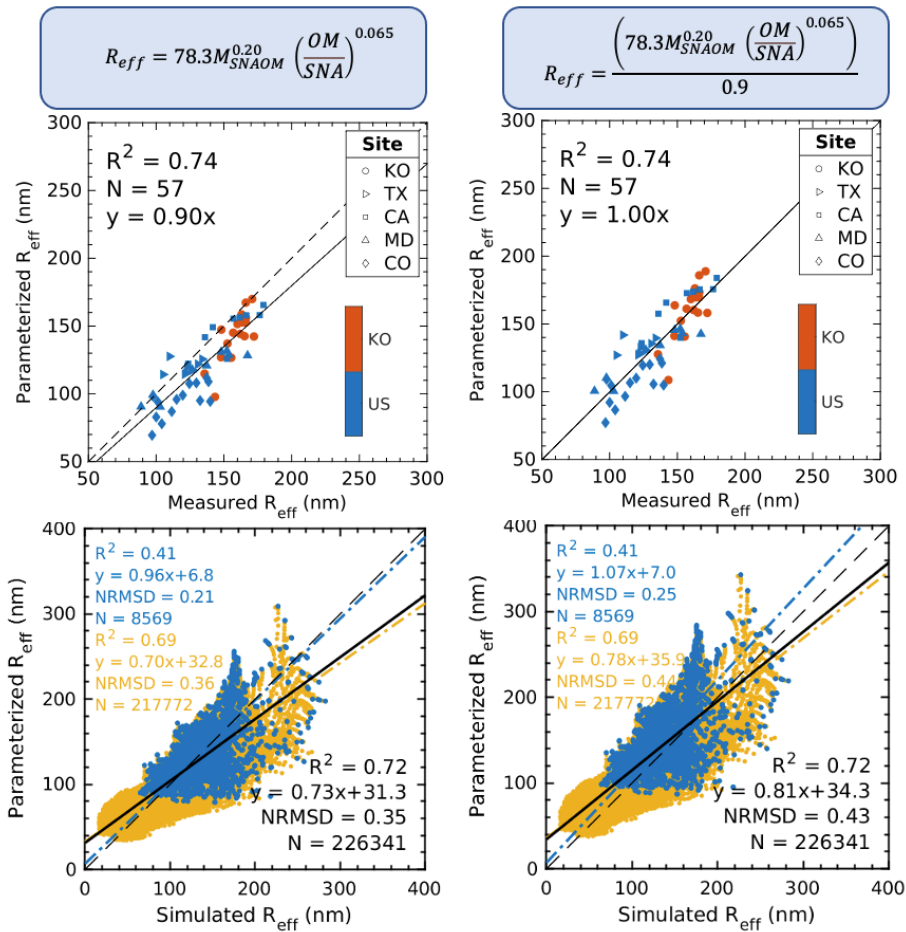
440 where subscript k indicates the property for the kth component. R_{eff} is the effective radius defined as the area weighted
 441 mean radius. Q_{ext} is the area-weighted mean extinction efficiency. M is the aerosol mass loading per unit volume. ρ is
 442 the aerosol density. Aerosol optical depth (AOD) is the integral of aerosol extinction across the vertical domain.

443 For each component, extinction is calculated for assumed log-normal size distribution with corresponding dry
 444 geometric mean radius R_g and geometric standard deviation σ , hygroscopicity, refractive index (RI), and density (ρ)
 445 for individual aerosol components, as listed in Table A1. Sulfate, nitrate, and ammonium are grouped into SNA for
 446 convenience. R_{eff} and Q_{ext} are calculated using Mie Theory (Mishchenko et al., 1999, 2002) based on assumptions in
 447 aerosol size and RI. Hygroscopicity for SNA and OM is represented using a κ -Kohler hygroscopic growth scheme
 448 (Kreidenweis et al., 2008) as implemented by (Latimer and Martin, 2019).

449 **Table A1. Dry aerosol properties in GEOS-Chem bulk model**

Aerosol components	R_g , μm	σ	Hygroscopicity	Refractive Index (dry, 550 nm)	ρ , g cm^{-3}	R_{eff} , μm	Q_{ext}
SNA	0.058	1.6	$\kappa = 0.61$	$1.53 - 6.0 \times 10^{-3}i$	1.7	0.101	0.603
OM	0.058	1.6	$\kappa = 0.1$	$1.53 - 6.0 \times 10^{-3}i$	1.3	0.101	0.603

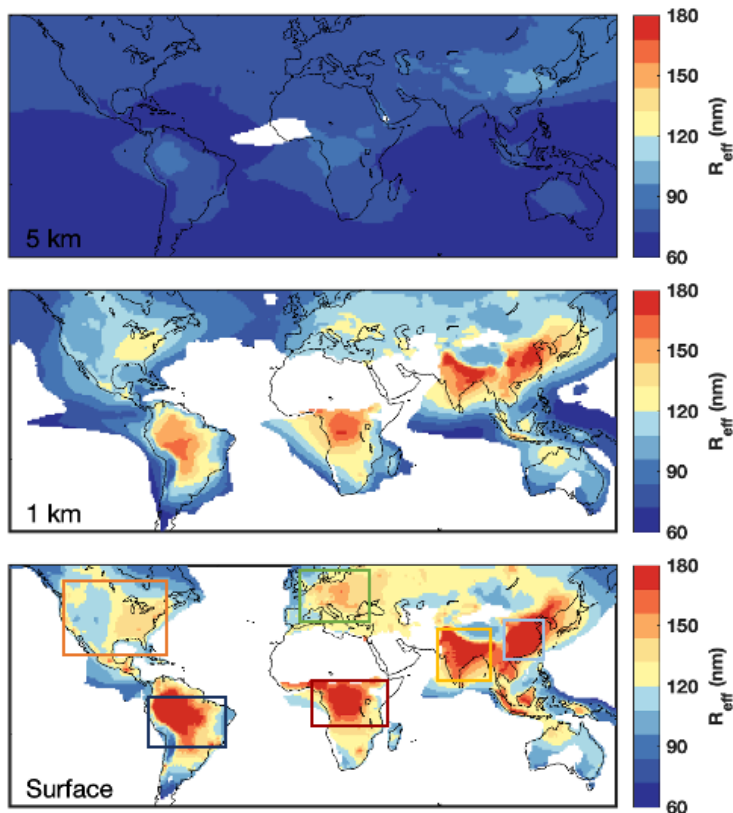
450



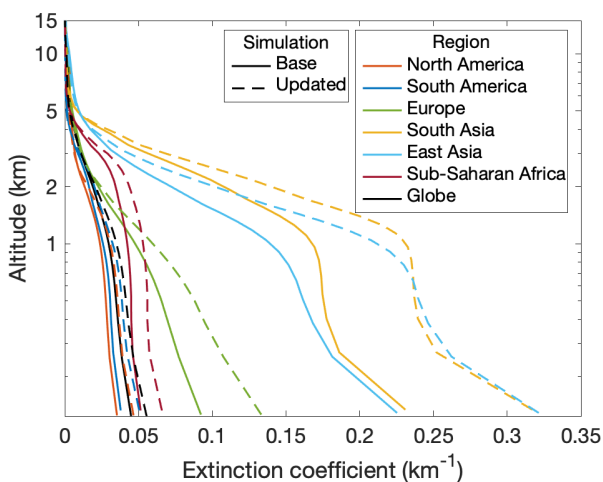
452

453 **Figure B1. (Top) Scatter plot of parameterized R_{eff} and measured R_{eff} from DISCOVER-AQ and KORUS-**
 454 **AQ. Each point represents a daily mean measurement. (Bottom) Scatter plot of parameterized R_{eff} and**
 455 **GEOS-Chem-TOMAS simulated R_{eff} for the planetary boundary layer (blue dots, line, and texts), and for the**
 456 **free troposphere (yellow dots, line, and texts). Black solid lines and the texts indicate the entire troposphere**
 457 **with the sum of SNA and OM > 90% of aerosol mass. The 1:1 line is dashed. NRMSD is the normalized root**
 458 **mean square deviation between the two datasets. N is the number of points in each dataset. The left panel**
 459 **indicates the original parameterization from multiple linear regression. The right panel shows the adjusted**
 460 **parameterization using aircraft measurements.**

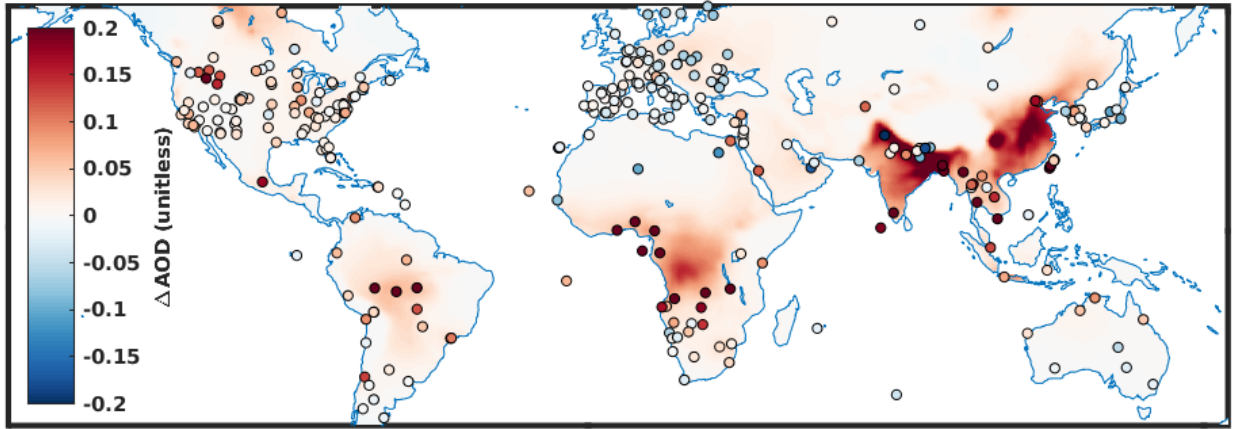
461



462
 463 **Figure B2.** Annual mean R_{eff} for SNA and OM at (top) about 5 km, (middle) about 1 km, and (bottom)
 464 surface, calculated using Eqn. (5) and simulated SNA and OM mass from GEOS-Chem bulk model. R_{eff} is
 465 shown only if M_{SNAOM} is greater than 80% of the total aerosol mass. Boxes in the bottom panel define regions
 466 referred to in Figure B3.



467
 468 **Figure B3.** Global and regional aerosol extinction coefficient simulated by GEOS-Chem bulk model with
 469 original R_{eff} (solid lines) and parameterized R_{eff} (dashed lines). Regions are defined by the boxes in Figure B2.



470

471 **Figure B4. Difference between AERONET AOD minus default GEOS-Chem simulated AOD (dots) and**
472 **difference between simulated AOD with the parameterized R_{eff} minus AOD with default R_{eff} (background).**

473 **Reference**

- 474 Aalto, P., Hämeri, K., Becker, E. D. O., Weber, R., Salm, J., Mäkelä, J. M., Hoell, C., O'Dowd, C. D., Karlsson, H.,
475 Hansson, H., Väkevä, M., Koponen, I. K., Buzorius, G., and Kulmala, M.: Physical characterization of aerosol
476 particles during nucleation events, *Tellus B Chem Phys Meteorol*, 53, 344–358,
477 <https://doi.org/10.3402/tellusb.v53i4.17127>, 2001.
- 478 AboEl-Fetouh, Y., O'Neill, N. T., Kodros, J. K., Pierce, J. R., Lu, H., Ranjbar, K., and Xian, P.: Seasonal comparisons
479 of GEOS-Chem-TOMAS (GCT) simulations with AERONET-inversion retrievals over sites in the North American
480 and European Arctic, *Atmos Environ*, 271, 118852, <https://doi.org/https://doi.org/10.1016/j.atmosenv.2021.118852>,
481 2022.
- 482 Adams, P. J. and Seinfeld, J. H.: Predicting global aerosol size distributions in general circulation models, *Journal of*
483 *Geophysical Research Atmospheres*, 107, AAC 4-1-AAC 4-23, <https://doi.org/10.1029/2001JD001010>, 2002.
- 484 Adams, P. J. and Seinfeld, J. H.: Disproportionate impact of particulate emissions on global cloud condensation nuclei
485 concentrations, *Geophys Res Lett*, 30, 1–4, <https://doi.org/10.1029/2002gl016303>, 2003.
- 486 Andreae, M. O., Acevedo, O. C., Araùjo, A., Artaxo, P., Barbosa, C. G. G., Barbosa, H. M. J., Brito, J., Carbone, S.,
487 Chi, X., Cintra, B. B. L., Da Silva, N. F., Dias, N. L., Dias-Júnior, C. Q., Ditas, F., Ditz, R., Godoi, A. F. L., Godoi,
488 R. H. M., Heimann, M., Hoffmann, T., Kesselmeier, J., Könemann, T., Krüger, M. L., Lavric, J. V., Manzi, A. O.,
489 Lopes, A. P., Martins, D. L., Mikhailov, E. F., Moran-Zuloaga, D., Nelson, B. W., Nölscher, A. C., Santos Nogueira,
490 D., Piedade, M. T. F., Pöhlker, C., Pöschl, U., Quesada, C. A., Rizzo, L. V., Ro, C. U., Ruckteschler, N., Sá, L. D. A.,
491 De Oliveira Sá, M., Sales, C. B., Dos Santos, R. M. N., Saturno, J., Schöngart, J., Sörgel, M., De Souza, C. M., De
492 Souza, R. A. F., Su, H., Targhetta, N., Tóta, J., Trebs, I., Trumbore, S., Van Eijck, A., Walter, D., Wang, Z., Weber,
493 B., Williams, J., Winderlich, J., Wittmann, F., Wolff, S., and Yáñez-Serrano, A. M.: The Amazon Tall Tower
494 Observatory (ATTO): Overview of pilot measurements on ecosystem ecology, meteorology, trace gases, and aerosols,
495 *Atmos Chem Phys*, 15, 10723–10776, <https://doi.org/10.5194/acp-15-10723-2015>, 2015.
- 496 Asmi, A., Wiedensohler, A., Laj, P., Fjaeraa, A. M., Sellegri, K., Birmili, W., Weingartner, E., Baltensperger, U.,
497 Zdimal, V., Zikova, N., Putaud, J. P., Marinoni, A., Tunved, P., Hansson, H. C., Fiebig, M., Kivekäs, N., Lihavainen,
498 H., Asmi, E., Ulevicius, V., Aalto, P. P., Swietlicki, E., Kristensson, A., Mihalopoulos, N., Kalivitis, N., Kalapov, I.,
499 Kiss, G., de Leeuw, G., Henzing, B., Harrison, R. M., Beddows, D., O'Dowd, C., Jennings, S. G., Flentje, H.,
500 Weinhold, K., Meinhardt, F., Ries, L., and Kulmala, M.: Number size distributions and seasonality of submicron
501 particles in Europe 2008-2009, *Atmos Chem Phys*, 11, 5505–5538, <https://doi.org/10.5194/acp-11-5505-2011>, 2011.
- 502 Bahreini, R., Jimenez, J. L., Wang, J., Flagan, R. C., Seinfeld, J. H., Jayne, J. T., and Worsnop, D. R.: Aircraft-based
503 aerosol size and composition measurements during ACE-Asia using an Aerodyne aerosol mass spectrometer, *Journal*
504 *of Geophysical Research: Atmospheres*, 108, <https://doi.org/10.1029/2002jd003226>, 2003.
- 505 Bindle, L., Martin, R. V., Cooper, M. J., Lundgren, E. W., Eastham, S. D., Auer, B. M., Clune, T. L., Weng, H., Lin,
506 J., Murray, L. T., Meng, J., Keller, C. A., Putman, W. M., Pawson, S., and Jacob, D. J.: Grid-stretching capability for

507 the GEOS-Chem 13.0.0 atmospheric chemistry model, *Geosci Model Dev*, 14, 5977–5997,
508 <https://doi.org/10.5194/gmd-14-5977-2021>, 2021.

509 Canagaratna, M. R., Jayne, J. T., Jimenez, J. L., Allan, J. D., Alfarra, M. R., Zhang, Q., Onasch, T. B., Drewnick, F.,
510 Coe, H., and Middlebrook, A.: Chemical and microphysical characterization of ambient aerosols with the aerodyne
511 aerosol mass spectrometer, *Mass Spectrom Rev*, 26, 185–222, <https://doi.org/doi:10.1002/mas.20115>, 2007.

512 Canagaratna, M. R., Jimenez, J. L., Kroll, J. H., Chen, Q., Kessler, S. H., Massoli, P., Hildebrandt Ruiz, L., Fortner,
513 E., Williams, L. R., Wilson, K. R., Surratt, J. D., Donahue, N. M., Jayne, J. T., and Worsnop, D. R.: Elemental ratio
514 measurements of organic compounds using aerosol mass spectrometry: Characterization, improved calibration, and
515 implications, *Atmos Chem Phys*, 15, 253–272, <https://doi.org/10.5194/acp-15-253-2015>, 2015.

516 Choi, S., Lamsal, L. N., Follette-Cook, M., Joiner, J., Krotkov, N. A., Swartz, W. H., Pickering, K. E., Loughner, C.
517 P., Appel, W., Pfister, G., Saide, P. E., Cohen, R. C., Weinheimer, A. J., and Herman, J. R.: Assessment of NO₂
518 observations during DISCOVER-AQ and KORUS-AQ field campaigns, *Atmos Meas Tech*, 13, 2523–2546,
519 <https://doi.org/10.5194/amt-13-2523-2020>, 2020.

520 Chu, D. A., Ferrare, R., Szykman, J., Lewis, J., Scarino, A., Hains, J., Burton, S., Chen, G., Tsai, T., Hostetler, C.,
521 Hair, J., Holben, B., and Crawford, J.: Regional characteristics of the relationship between columnar AOD and surface
522 PM_{2.5}: Application of lidar aerosol extinction profiles over Baltimore-Washington Corridor during DISCOVER-AQ,
523 *Atmos Environ*, 101, 338e349-349, <https://doi.org/10.1016/j.atmosenv.2014.11.034>, 2015.

524 Croft, B., Lohmann, U., and von Salzen, K.: Black carbon ageing in the Canadian Centre for Climate modelling and
525 analysis atmospheric general circulation model, *Atmos Chem Phys*, 5, 1931–1949, [https://doi.org/10.5194/acp-5-](https://doi.org/10.5194/acp-5-1931-2005)
526 1931-2005, 2005.

527 D’Andrea, S. D., Häkkinen, S. A. K., Westervelt, D. M., Kuang, C., Levin, E. J. T., Kanawade, V. P., Leaitch, W. R.,
528 Spracklen, D. V., Riipinen, I., and Pierce, J. R.: Understanding global secondary organic aerosol amount and size-
529 resolved condensational behavior, *Atmos Chem Phys*, 13, 11519–11534, <https://doi.org/10.5194/acp-13-11519-2013>,
530 2013.

531 Dibb, J. E., Talbot, R. W., Scheuer, E. M., Seid, G., Avery, M. A., and Singh, H. B.: Aerosol chemical composition
532 in Asian continental outflow during the TRACE-P campaign: Comparison with PEM-West B, *Journal of Geophysical*
533 *Research: Atmospheres*, 108, <https://doi.org/10.1029/2002jd003111>, 2003.

534 Van Donkelaar, A., Martin, R. V., Li, C., and Burnett, R. T.: Regional Estimates of Chemical Composition of Fine
535 Particulate Matter Using a Combined Geoscience-Statistical Method with Information from Satellites, Models, and
536 Monitors, *Environ Sci Technol*, 53, 2595–2611, <https://doi.org/10.1021/acs.est.8b06392>, 2019.

537 Eastham, S. D., Long, M. S., Keller, C. A., Lundgren, E., Yantosca, R. M., Zhuang, J., Li, C., Lee, C. J., Yannetti, M.,
538 Auer, B. M., Clune, T. L., Kouatchou, J., Putman, W. M., Thompson, M. A., Trayanov, A. L., Molod, A. M., Martin,
539 R. V., and Jacob, D. J.: GEOS-Chem high performance (GCHP v11-02c): A next-generation implementation of the

540 GEOS-Chem chemical transport model for massively parallel applications, *Geosci Model Dev*, 11, 2941–2953,
541 <https://doi.org/10.5194/gmd-11-2941-2018>, 2018.

542 Emerson, E. W., Hodshire, A. L., DeBolt, H. M., Bilsback, K. R., Pierce, J. R., McMeeking, G. R., and Farmer, D. K.:
543 Revisiting particle dry deposition and its role in radiative effect estimates, *Proc Natl Acad Sci U S A*, 117, 26076–
544 26082, <https://doi.org/10.1073/pnas.2014761117>, 2020.

545 Ervens, B., Turpin, B. J., and Weber, R. J.: Secondary organic aerosol formation in cloud droplets and aqueous
546 particles (aqSOA): A review of laboratory, field and model studies, *Atmos Chem Phys*, 11, 11069–11102,
547 <https://doi.org/10.5194/acp-11-11069-2011>, 2011.

548 Estillore, A. D., Trueblood, J. V., and Grassian, V. H.: Atmospheric chemistry of bioaerosols: Heterogeneous and
549 multiphase reactions with atmospheric oxidants and other trace gases, *Chem Sci*, 7, 6604–6616,
550 <https://doi.org/10.1039/c6sc02353c>, 2016.

551 Fairlie, D. T., Jacob, D. J., and Park, R. J.: The impact of transpacific transport of mineral dust in the United States,
552 *Atmos Environ*, 41, 1251–1266, <https://doi.org/10.1016/j.atmosenv.2006.09.048>, 2007.

553 Faxvog, F. R. and Roessler, D. M.: Carbon aerosol visibility vs particle size distribution, *Appl Opt*, 17, 2612,
554 <https://doi.org/10.1364/ao.17.002612>, 1978.

555 Fountoukis, C. and Nenes, A.: ISORROPIAII: A computationally efficient thermodynamic equilibrium model for K+
556 Ca2+-Mg2+-NH4+-Na+-SO4--NO3--Cl--H2O aerosols, *Atmos Chem Phys*, 7, 4639–4659,
557 <https://doi.org/10.5194/acp-7-4639-2007>, 2007.

558 GCST, Yu, F., and Luo, G.: APM aerosol microphysics, http://wiki.seas.harvard.edu/geos-chem/index.php/APM_aerosol_microphysics, last access: 23 January, 2023.

560 Geng, G., Zhang, Q., Tong, D., Li, M., Zheng, Y., Wang, S., and He, K.: Chemical composition of ambient PM_{2.5}
561 over China and relationship to precursor emissions during 2005-2012, *Atmos Chem Phys*, 17, 9187–9203,
562 <https://doi.org/10.5194/acp-17-9187-2017>, 2017.

563 Giles, D. M., Sinyuk, A., Sorokin, M. G., Schafer, J. S., Smirnov, A., Slutsker, I., Eck, T. F., Holben, B. N., Lewis, J.
564 R., Campbell, J. R., Welton, E. J., Korkin, S. V., and Lyapustin, A. I.: Advancements in the Aerosol Robotic Network
565 (AERONET) Version 3 database - Automated near-real-time quality control algorithm with improved cloud screening
566 for Sun photometer aerosol optical depth (AOD) measurements, *Atmos Meas Tech*, 12, 169–209,
567 <https://doi.org/10.5194/amt-12-169-2019>, 2019.

568 Guo, H., Campuzano-Jost, P., Nault, B. A., Day, D. A., Schroder, J. C., Kim, D., Dibb, J. E., Dollner, M., Weinzierl,
569 B., and Jimenez, J. L.: The importance of size ranges in aerosol instrument intercomparisons: A case study for the
570 Atmospheric Tomography Mission, *Atmos Meas Tech*, 14, 3631–3655, <https://doi.org/10.5194/amt-14-3631-2021>,
571 2021.

572 Hair, J. W., Hostetler, C. A., Cook, A. L., Harper, D. B., Ferrare, R. A., Mack, T. L., Welch, W., Izquierdo, L. R., and
573 Hovis, F. E.: Airborne High Spectral Resolution Lidar for profiling Aerosol optical properties, *Appl Opt*, 47, 6734–
574 6753, <https://doi.org/10.1364/AO.47.006734>, 2008.

575 Hammer, M. S., Martin, R. V., Van Donkelaar, A., Buchard, V., Torres, O., Ridley, D. A., and Spurr, R. J. D.:
576 Interpreting the ultraviolet aerosol index observed with the OMI satellite instrument to understand absorption by
577 organic aerosols: Implications for atmospheric oxidation and direct radiative effects, *Atmos Chem Phys*, 16, 2507–
578 2523, <https://doi.org/10.5194/acp-16-2507-2016>, 2016.

579 Hansen, J. E. and Travis, L. D.: Light scattering in planetary atmospheres, *Space Sci Rev*, 16, 527–610,
580 <https://doi.org/10.1007/BF00168069>, 1974.

581 Hayes, P. L., Ortega, A. M., Cubison, M. J., Froyd, K. D., Zhao, Y., Cliff, S. S., Hu, W. W., Toohey, D. W., Flynn, J.
582 H., Lefer, B. L., Grossberg, N., Alvarez, S., Rappenglück, B., Taylor, J. W., Allan, J. D., Holloway, J. S., Gilman, J.
583 B., Kuster, W. C., De Gouw, J. A., Massoli, P., Zhang, X., Liu, J., Weber, R. J., Corrigan, A. L., Russell, L. M.,
584 Isaacman, G., Worton, D. R., Kreisberg, N. M., Goldstein, A. H., Thalman, R., Waxman, E. M., Volkamer, R., Lin,
585 Y. H., Surratt, J. D., Kleindienst, T. E., Offenberg, J. H., Dusanter, S., Griffith, S., Stevens, P. S., Brioude, J., Angevine,
586 W. M., and Jimenez, J. L.: Organic aerosol composition and sources in Pasadena, California, during the 2010 CalNex
587 campaign, *Journal of Geophysical Research Atmospheres*, 118, 9233–9257, <https://doi.org/10.1002/jgrd.50530>, 2013.

588 Hinds, W. C. and Zhu, Y.: *Aerosol technology: Properties, behavior, and measurement of airborne particles*, Second.,
589 Wiley, New York, 1999.

590 Huang, Y., Li, L., Li, J., Wang, X., Chen, H., Chen, J., Yang, X., Gross, D. S., Wang, H., Qiao, L., and Chen, C.: A
591 case study of the highly time-resolved evolution of aerosol chemical and optical properties in urban Shanghai, China,
592 *Atmos Chem Phys*, 13, 3931–3944, <https://doi.org/10.5194/acp-13-3931-2013>, 2013.

593 Jaeglé, L., Quinn, P. K., Bates, T. S., Alexander, B., and Lin, J. T.: Global distribution of sea salt aerosols: New
594 constraints from in situ and remote sensing observations, *Atmos Chem Phys*, 11, 3137–3157,
595 <https://doi.org/10.5194/acp-11-3137-2011>, 2011.

596 Janháall, S., Andreae, M. O., and Pöschl, U.: Biomass burning aerosol emissions from vegetation fires: Particle number
597 and mass emission factors and size distributions, *Atmos Chem Phys*, 10, 1427–1439, <https://doi.org/10.5194/acp-10-1427-2010>, 2010.

599 Jin, J., Henzing, B., and Segers, A.: How aerosol size matters in aerosol optical depth (AOD) assimilation and the
600 optimization using the Ångström exponent, *Atmos Chem Phys*, 23, 1641–1660, <https://doi.org/10.5194/acp-23-1641-2023>, 2023.

602 Jordan, C. E., Crawford, J. H., Beyersdorf, A. J., Eck, T. F., Halliday, H. S., Nault, B. A., Chang, L.-S., Park, J., Park,
603 R., and Lee, G.: Investigation of factors controlling PM_{2.5} variability across the South Korean Peninsula during
604 KORUS-AQ, *Elementa: Science of the Anthropocene*, 8, 2020.

605 Kahn, R. A., Gaitley, B. J., Martonchik, J. v., Diner, D. J., Crean, K. A., and Holben, B.: Multiangle Imaging
606 Spectroradiometer (MISR) global aerosol optical depth validation based on 2 years of coincident Aerosol Robotic
607 Network (AERONET) observations, *Journal of Geophysical Research D: Atmospheres*, 110, 1–16,
608 <https://doi.org/10.1029/2004JD004706>, 2005.

609 Karydis, V. A., Kumar, P., Barahona, D., Sokolik, I. N., and Nenes, A.: On the effect of dust particles on global cloud
610 condensation nuclei and cloud droplet number, *Journal of Geophysical Research Atmospheres*, 116,
611 <https://doi.org/10.1029/2011JD016283>, 2011.

612 Kellogg, W. W.: *Aerosols and Climate.*, *Science* (1979), 183, 281–296,
613 <https://doi.org/10.1093/oso/9780198779308.003.0005>, 1980.

614 Kodros, J. K. and Pierce, J. R.: Important global and regional differences in aerosol cloud-albedo effect estimates
615 between simulations with and without prognostic aerosol microphysics, *J Geophys Res*, 122, 4003–4018,
616 <https://doi.org/10.1002/2016JD025886>, 2017.

617 Kodros, J. K., Volckens, J., Jathar, S. H., and Pierce, J. R.: Ambient particulate matter size distributions drive regional
618 and global variability in particle deposition in the respiratory tract, *Geohealth*, 2, 298–312,
619 <https://doi.org/10.1029/2018gh000145>, 2018.

620 Koffi, B., Schulz, M., Bréon, F. M., Dentener, F., Steensen, B. M., Griesfeller, J., Winker, D., Balkanski, Y., Bauer,
621 S. E., Bellouin, N., Bernsten, T., Bian, H., Chin, M., Diehl, T., Easter, R., Ghan, S., Hauglustaine, D. A., Iversen, T.,
622 Kirkevåg, A., Liu, X., Lohmann, U., Myhre, G., Rasch, P., Seland, Ø., Skeie, R. B., Steenrod, S. D., Stier, P., Tackett,
623 J., Takemura, T., Tsigaridis, K., Vuolo, M. R., Yoon, J., and Zhang, K.: Evaluation of the aerosol vertical distribution
624 in global aerosol models through comparison against CALIOP measurements: AeroCom phase II results, *J Geophys*
625 *Res*, 121, 7254–7283, <https://doi.org/10.1002/2015JD024639>, 2016.

626 Kopke P., H. M. S. I. S. E. P.: Aerosol data set, Max Planck Institut fur Meteorologie, Report No. 243, Hamburg,
627 <https://doi.org/Report No. 243>, 1997.

628 Kreidenweis, S. M., Petters, M. D., and DeMott, P. J.: Single-parameter estimates of aerosol water content,
629 *Environmental Research Letters*, 3, 35002, 2008.

630 Lamarque, J. F., Shindell, D. T., Josse, B., Young, P. J., Cionni, I., Eyring, V., Bergmann, D., Cameron-Smith, P.,
631 Collins, W. J., Doherty, R., Dalsoren, S., Faluvegi, G., Folberth, G., Ghan, S. J., Horowitz, L. W., Lee, Y. H.,
632 MacKenzie, I. A., Nagashima, T., Naik, V., Plummer, D., Righi, M., Rumbold, S. T., Schulz, M., Skeie, R. B.,
633 Stevenson, D. S., Strode, S., Sudo, K., Szopa, S., Voulgarakis, A., and Zeng, G.: The atmospheric chemistry and
634 climate model intercomparison Project (ACCMIP): Overview and description of models, simulations and climate
635 diagnostics, *Geosci Model Dev*, 6, 179–206, <https://doi.org/10.5194/gmd-6-179-2013>, 2013.

636 Lamb, K. D., Perring, A. E., Samset, B., Peterson, D., Davis, S., Anderson, B. E., Beyersdorf, A., Blake, D. R.,
637 Campuzano-Jost, P., Corr, C. A., Diskin, G. S., Kondo, Y., Moteki, N., Nault, B. A., Oh, J., Park, M., Pusede, S. E.,
638 Simpson, I. J., Thornhill, K. L., Wisthaler, A., and Schwarz, J. P.: Estimating Source Region Influences on Black

639 Carbon Abundance, Microphysics, and Radiative Effect Observed Over South Korea, *Journal of Geophysical*
640 *Research: Atmospheres*, 123, 13,527–13,548, <https://doi.org/10.1029/2018JD029257>, 2018.

641 Latimer, R. N. C. and Martin, R. v.: Interpretation of measured aerosol mass scattering efficiency over North America
642 using a chemical transport model, *Atmos Chem Phys*, 19, 2635–2653, <https://doi.org/10.5194/acp-19-2635-2019>,
643 2019.

644 Lee, Y. N., Weber, R., Ma, Y., Orsini, D., Maxwell-Meier, K., Blake, D., Meinardi, S., Sachse, G., Harward, C., Chen,
645 T. Y., Thornton, D., Tu, F. H., and Bandy, A.: Airborne measurement of inorganic ionic components of fine aerosol
646 particles using the particle-into-liquid sampler coupled to ion chromatography technique during ACE-Asia and
647 TRACE-P, *Journal of Geophysical Research: Atmospheres*, 108, <https://doi.org/10.1029/2002jd003265>, 2003.

648 Levy, R. C., Mattoo, S., Munchak, L. A., Remer, L. A., Sayer, A. M., Patadia, F., and Hsu, N. C.: The Collection 6
649 MODIS aerosol products over land and ocean, *Atmos Meas Tech*, 6, 2989–3034, [https://doi.org/10.5194/amt-6-2989-](https://doi.org/10.5194/amt-6-2989-2013)
650 2013, 2013.

651 Li, C., Martin, R. V., van Donkelaar, A., Boys, B. L., Hammer, M. S., Xu, J.-W., Marais, E. A., Reff, A., Strum, M.,
652 and Ridley, D. A.: Trends in chemical composition of global and regional population-weighted fine particulate matter
653 estimated for 25 years, *Environ Sci Technol*, 51, 11185–11195, 2017.

654 Liu, H., Jacob, D. J., Bey, I., and Yantosca, R. M.: Constraints from 210Pb and 7Be on wet deposition and transport
655 in a global three-dimensional chemical tracer model driven by assimilated meteorological fields, *Journal of*
656 *Geophysical Research Atmospheres*, 106, 12109–12128, <https://doi.org/10.1029/2000JD900839>, 2001.

657 Liu, X., Easter, R. C., Ghan, S. J., Zaveri, R., Rasch, P., Shi, X., Lamarque, J. F., Gettelman, A., Morrison, H., Vitt,
658 F., Conley, A., Park, S., Neale, R., Hannay, C., Ekman, A. M. L., Hess, P., Mahowald, N., Collins, W., Iacono, M. J.,
659 Bretherton, C. S., Flanner, M. G., and Mitchell, D.: Toward a minimal representation of aerosols in climate models:
660 Description and evaluation in the Community Atmosphere Model CAM5, *Geosci Model Dev*, 5, 709–739,
661 <https://doi.org/10.5194/gmd-5-709-2012>, 2012.

662 Liu, X., Ma, P.-L., Wang, H., Tilmes, S., Singh, B., Easter, R. C., Ghan, S. J., and Rasch, P. J.: Description and
663 evaluation of a new four-mode version of the Modal Aerosol Module (MAM4) within version 5.3 of the Community
664 Atmosphere Model, *Geosci Model Dev*, 9, 505–522, 2016.

665 Lyapustin, A., Wang, Y., Korkin, S., and Huang, D.: MODIS Collection 6 MAIAC algorithm, *Atmos Meas Tech*, 11,
666 5741–5765, <https://doi.org/10.5194/amt-11-5741-2018>, 2018.

667 Malm, W. C., Sisler, J. F., Huffman, D., Eldred, R. A., and Cahill, T. A.: Spatial and seasonal trends in particle
668 concentration and optical extinction in the United States, *J Geophys Res*, 99, 1347–1370,
669 <https://doi.org/10.1029/93JD02916>, 1994.

670 Mann, G. W., Carslaw, K. S., Spracklen, D. V., Ridley, D. A., Manktelow, P. T., Chipperfield, M. P., Pickering, S. J.,
671 and Johnson, C. E.: Description and evaluation of GLOMAP-mode: A modal global aerosol microphysics model for

672 the UKCA composition-climate model, *Geosci Model Dev*, 3, 519–551, <https://doi.org/10.5194/gmd-3-519-2010>,
673 2010.

674 Marais, E. A., Jacob, D. J., Jimenez, J. L., Campuzano-Jost, P., Day, D. A., Hu, W., Krechmer, J., Zhu, L., Kim, P. S.,
675 Miller, C. C., Fisher, J. A., Travis, K., Yu, K., Hanisco, T. F., Wolfe, G. M., Arkinson, H. L., Pye, H. O. T., Froyd, K.
676 D., Liao, J., and McNeill, V. F.: Aqueous-phase mechanism for secondary organic aerosol formation from isoprene:
677 Application to the southeast United States and co-benefit of SO₂ emission controls, *Atmos Chem Phys*, 16, 1603–
678 1618, <https://doi.org/10.5194/acp-16-1603-2016>, 2016.

679 Martin, R. V., Jacob, D. J., Yantosca, R. M., Chin, M., and Ginoux, P.: Global and regional decreases in tropospheric
680 oxidants from photochemical effects of aerosols, *Journal of Geophysical Research: Atmospheres*, 108,
681 <https://doi.org/10.1029/2002jd002622>, 2003.

682 Martin, R. V., Eastham, S. D., Bindle, L., Lundgren, E. W., Clune, T. L., Keller, C. A., Downs, W., Zhang, D., Lucchesi,
683 R. A., Sulprizio, M. P., Yantosca, R. M., Li, Y., Estrada, L., Putman, W. M., Auer, B. M., Trayanov, L., Pawson, S.,
684 and Jacob, D. J.: Improved Advection , Resolution , Performance , and Community Access in the New Generation
685 (Version 13) of the High Performance GEOS-Chem Global Atmospheric Chemistry Model (GCHP), *Geoscientific*
686 *Model Development Discussions*, 720, 1–30, <https://doi.org/10.5194/gmd-2022-42>, 2022.

687 McDuffie, E. E., Smith, S. J., O'Rourke, P., Tibrewal, K., Venkataraman, C., Marais, E. A., Zheng, B., Crippa, M.,
688 Brauer, M., and Martin, R. V.: A global anthropogenic emission inventory of atmospheric pollutants from sector- And
689 fuel-specific sources (1970-2017): An application of the Community Emissions Data System (CEDS), *Earth Syst Sci*
690 *Data*, 12, 3413–3442, <https://doi.org/10.5194/essd-12-3413-2020>, 2020.

691 McDuffie, E. E., Martin, R. V., Spadaro, J. V., Burnett, R., Smith, S. J., O'Rourke, P., Hammer, M. S., van Donkelaar,
692 A., Bindle, L., Shah, V., Jaeglé, L., Luo, G., Yu, F., Adeniran, J. A., Lin, J., and Brauer, M.: Source sector and fuel
693 contributions to ambient PM_{2.5} and attributable mortality across multiple spatial scales, *Nat Commun*, 12, 1–12,
694 <https://doi.org/10.1038/s41467-021-23853-y>, 2021.

695 McNaughton, C. S., Clarke, A. D., Howell, S. G., Pinkerton, M., Anderson, B., Thornhill, L., Hudgins, C., Winstead,
696 E., Dibb, J. E., Scheuer, E., and Maring, H.: Results from the DC-8 inlet characterization experiment (DICE): Airborne
697 versus surface sampling of mineral dust and sea salt aerosols, *Aerosol Science and Technology*, 41, 136–159,
698 <https://doi.org/10.1080/02786820601118406>, 2007.

699 Meng, J., Martin, R. V., Li, C., Van Donkelaar, A., Tzompa-Sosa, Z. A., Yue, X., Xu, J. W., Weagle, C. L., and
700 Burnett, R. T.: Source Contributions to Ambient Fine Particulate Matter for Canada, *Environ Sci Technol*, 53, 10269–
701 10278, <https://doi.org/10.1021/acs.est.9b02461>, 2019.

702 Meng, J., Martin, R. v., Ginoux, P., Hammer, M., Sulprizio, M. P., Ridley, D. A., and van Donkelaar, A.: Grid-
703 independent high-resolution dust emissions (v1.0) for chemical transport models: Application to GEOS-Chem (12.5.0),
704 *Geosci Model Dev*, 14, 4249–4260, <https://doi.org/10.5194/gmd-14-4249-2021>, 2021a.

705 Meng, J., Martin, R. V., Ginoux, P., Hammer, M., Sulprizio, M. P., Ridley, D. A., and Van Donkelaar, A.: Grid-
706 independent high-resolution dust emissions (v1.0) for chemical transport models: Application to GEOS-Chem (12.5.0),
707 *Geosci Model Dev*, 14, 4249–4260, <https://doi.org/10.5194/gmd-14-4249-2021>, 2021b.

708 Mishchenko, M. I., Dlugach, J. M., Yanovitskij, E. G., and Zakharova, N. T.: Bidirectional reflectance of flat, optically
709 thick particulate layers: An efficient radiative transfer solution and applications to snow and soil surfaces, *J Quant*
710 *Spectrosc Radiat Transf*, 63, 409–432, [https://doi.org/10.1016/S0022-4073\(99\)00028-X](https://doi.org/10.1016/S0022-4073(99)00028-X), 1999.

711 Mishchenko, M. I., Travis, L. D., and Lacis, A. a: *Scattering, Absorption, and Emission of Light by Small Particles*,
712 Cambridge University Press, Cambridge, 1–486 pp., 2002.

713 Moore, R. H., Wiggins, E. B., Ahern, A. T., Zimmerman, S., Montgomery, L., Campuzano Jost, P., Robinson, C. E.,
714 Ziemba, L. D., Winstead, E. L., Anderson, B. E., Brock, C. A., Brown, M. D., Chen, G., Crosbie, E. C., Guo, H.,
715 Jimenez, J. L., Jordan, C. E., Lyu, M., Nault, B. A., Rothfuss, N. E., Sanchez, K. J., Schueneman, M., Shingler, T. J.,
716 Shook, M. A., Thornhill, K. L., Wagner, N. L., and Wang, J.: Sizing response of the Ultra-High Sensitivity Aerosol
717 Spectrometer (UHSAS) and Laser Aerosol Spectrometer (LAS) to changes in submicron aerosol composition and
718 refractive index, *Atmos Meas Tech*, 14, 4517–4542, <https://doi.org/10.5194/amt-14-4517-2021>, 2021.

719 Napari, I., Noppel, M., Vehkamäki, H., and Kulmala, M.: Parametrization of ternary nucleation rates for H₂SO₄-NH₃-
720 H₂O vapors, *Journal of Geophysical Research Atmospheres*, 107, AAC 6-1-AAC 6-6,
721 <https://doi.org/10.1029/2002JD002132>, 2002.

722 Nault, B. A., Campuzano-Jost, P., Day, D. A., Schroder, J. C., Anderson, B., Beyersdorf, A. J., Blake, D. R., Brune,
723 W. H., Choi, Y., Corr, C. A., de Gouw, J. A., Dibb, J., Digangi, J. P., Diskin, G. S., Fried, A., Gregory Huey, L., Kim,
724 M. J., Knute, C. J., Lamb, K. D., Lee, T., Park, T., Pusede, S. E., Scheuer, E., Thornhill, K. L., Woo, J. H., and Jimenez,
725 J. L.: Secondary organic aerosol production from local emissions dominates the organic aerosol budget over Seoul,
726 South Korea, during KORUS-AQ, *Atmos Chem Phys*, 18, 17769–17800, <https://doi.org/10.5194/acp-18-17769-2018>,
727 2018.

728 Ngo, N. S., Asseko, S. V. J., Ebanega, M. O., Allo'o Allo'o, S. M., and Hystad, P.: The relationship among PM_{2.5},
729 traffic emissions, and socioeconomic status: Evidence from Gabon using low-cost, portable air quality monitors,
730 *Transp Res D Transp Environ*, 68, 2–9, <https://doi.org/10.1016/j.trd.2018.01.029>, 2019.

731 Park, R. J.: Natural and transboundary pollution influences on sulfate-nitrate-ammonium aerosols in the United States:
732 Implications for policy, *J Geophys Res*, 109, <https://doi.org/10.1029/2003jd004473>, 2004.

733 Park, R. J., Jacob, D. J., Chin, M., and Martin, R. V.: Sources of carbonaceous aerosols over the United States and
734 implications for natural visibility, *Journal of Geophysical Research Atmospheres*, 108,
735 <https://doi.org/10.1029/2002jd003190>, 2003.

736 Park, S.-S., Sim, S. Y., Bae, M.-S., and Schauer, J. J.: Size distribution of water-soluble components in particulate
737 matter emitted from biomass burning, *Atmos Environ*, 73, 62–72, 2013.

738 Philip, S., Martin, R. V., Pierce, J. R., Jimenez, J. L., Zhang, Q., Canagaratna, M. R., Spracklen, D. V., Nowlan, C.
739 R., Lamsal, L. N., Cooper, M. J., and Krotkov, N. A.: Spatially and seasonally resolved estimate of the ratio of organic
740 mass to organic carbon, *Atmos Environ*, 87, 34–40, <https://doi.org/10.1016/j.atmosenv.2013.11.065>, 2014.

741 Philip, S., Martin, R. V., Snider, G., Weagle, C. L., Van Donkelaar, A., Brauer, M., Henze, D. K., Klimont, Z.,
742 Venkataraman, C., Guttikunda, S. K., and Zhang, Q.: Anthropogenic fugitive, combustion and industrial dust is a
743 significant, underrepresented fine particulate matter source in global atmospheric models, *Environmental Research*
744 *Letters*, 12, <https://doi.org/10.1088/1748-9326/aa65a4>, 2017.

745 Pierce, J. R., Chen, K., and Adams, P. J.: Contribution of primary carbonaceous aerosol to cloud condensation nuclei:
746 Processes and uncertainties evaluated with a global aerosol microphysics model, *Atmos Chem Phys*, 7, 5447–5466,
747 <https://doi.org/10.5194/acp-7-5447-2007>, 2007.

748 Pierce, J. R., Croft, B., Kodros, J. K., D’Andrea, S. D., and Martin, R. V.: The importance of interstitial particle
749 scavenging by cloud droplets in shaping the remote aerosol size distribution and global aerosol-climate effects, *Atmos*
750 *Chem Phys*, 15, 6147–6158, <https://doi.org/10.5194/acp-15-6147-2015>, 2015.

751 Plaza, J., Pujadas, M., Gómez-Moreno, F. J., Sánchez, M., and Artíñano, B.: Mass size distributions of soluble sulfate,
752 nitrate and ammonium in the Madrid urban aerosol, *Atmos Environ*, 45, 4966–4976, 2011.

753 Podolske, J. R., Sachse, G. W., and Diskin, G. S.: Calibration and data retrieval algorithms for the NASA
754 Langley/Ames Diode Laser Hygrometer for the NASA Transport and Chemical Evolution over the Pacific (TRACE-
755 P) mission, *Journal of Geophysical Research: Atmospheres*, 108, <https://doi.org/10.1029/2002jd003156>, 2003.

756 Pye, H. O. T., Chan, A. W. H., Barkley, M. P., and Seinfeld, J. H.: Global modeling of organic aerosol: The importance
757 of reactive nitrogen (NO_x and NO₃), *Atmos Chem Phys*, 10, 11261–11276, [https://doi.org/10.5194/acp-10-11261-](https://doi.org/10.5194/acp-10-11261-2010)
758 2010, 2010.

759 Ramnarine, E., Kodros, J. K., Hodshire, A. L., Lonsdale, C. R., Alvarado, M. J., and Pierce, J. R.: Effects of near-
760 source coagulation of biomass burning aerosols on global predictions of aerosol size distributions and implications
761 for aerosol radiative effects, *Atmos Chem Phys*, 19, 6561–6577, <https://doi.org/10.5194/acp-19-6561-2019>, 2019.

762 Reid, J. S., Eck, T. F., Christopher, S. A., Koppman, R., Dubovik, O., Eleuterio, D. P., Holben, B. N., Reid, E. A., and
763 Zhang, J.: A review of biomass burning emissions part III: Intensive optical properties of biomass burning particles,
764 *Atmos Chem Phys*, 5, 827–849, <https://doi.org/10.5194/acp-5-827-2005>, 2005.

765 Remoundaki, E., Kassomenos, P., Mantas, E., Mihalopoulos, N., and Tsezos, M.: Composition and mass closure of
766 PM_{2.5} in urban environment (Athens, Greece), *Aerosol Air Qual Res*, 13, 72–82,
767 <https://doi.org/10.4209/aaqr.2012.03.0054>, 2013.

768 Reutter, P., Su, H., Trentmann, J., Simmel, M., Rose, D., Gunthe, S. S., Wernli, H., Andreae, M. O., and Pöschl, U.:
769 Aerosol- and updraft-limited regimes of cloud droplet formation: Influence of particle number, size and hygroscopicity
770 on the activation of cloud condensation nuclei (CCN), *Atmos Chem Phys*, 9, 7067–7080, [https://doi.org/10.5194/acp-](https://doi.org/10.5194/acp-9-7067-2009)
771 9-7067-2009, 2009.

772 Rissler, J., Vestin, A., Swietlicki, E., Fisch, G., Zhou, J., Artaxo, P., and Andreae, M. O.: Size distribution and
773 hygroscopic properties of aerosol particles from dry-season biomass burning in Amazonia, *Atmos Chem Phys*, 6, 471–
774 491, <https://doi.org/10.5194/acp-6-471-2006>, 2006.

775 Rodríguez, S., Van Dingenen, R., Putaud, J. P., Dell'Acqua, A., Pey, J., Querol, X., Alastuey, A., Chenery, S., Ho, K.
776 F., Harrison, R., Tardivo, R., Scarnato, B., and Gemelli, V.: A study on the relationship between mass concentrations,
777 chemistry and number size distribution of urban fine aerosols in Milan, Barcelona and London, *Atmos Chem Phys*, 7,
778 2217–2232, <https://doi.org/10.5194/acp-7-2217-2007>, 2007.

779 Ruijrok, W., Davidson, C. I., and Nicholson, K. W.: Dry deposition of particles, *Tellus B*, 47, 587–601,
780 <https://doi.org/10.1034/j.1600-0889.47.issue5.6.x>, 1995.

781 Sakamoto, K. M., Laing, J. R., Stevens, R. G., Jaffe, D. A., and Pierce, J. R.: The evolution of biomass-burning aerosol
782 size distributions due to coagulation: Dependence on fire and meteorological details and parameterization, *Atmos*
783 *Chem Phys*, 16, 7709–7724, <https://doi.org/10.5194/acp-16-7709-2016>, 2016.

784 Sawamura, P., Moore, H. R., Burton, P. S., Chemyakin, E., Müller, D., Kolgotin, A., Ferrare, A. R., Hostetler, A. C.,
785 Ziemba, D. L., Beyersdorf, J. A., and Anderson, E. B.: HSRL-2 aerosol optical measurements and microphysical
786 retrievals vs. airborne in situ measurements during DISCOVER-AQ 2013: An intercomparison study, *Atmos Chem*
787 *Phys*, 17, 7229–7243, <https://doi.org/10.5194/acp-17-7229-2017>, 2017.

788 Schubert, S. D., Rood, R. B., and Pfaendtner, J.: An Assimilated Dataset for Earth Science Applications, *Bull Am*
789 *Meteorol Soc*, 74, 2331–2342, [https://doi.org/10.1175/1520-0477\(1993\)074<2331:AADFES>2.0.CO;2](https://doi.org/10.1175/1520-0477(1993)074<2331:AADFES>2.0.CO;2), 1993.

790 Schwarz, J. P., Gao, R. S., Fahey, D. W., Thomson, D. S., Watts, L. A., Wilson, J. C., Reeves, J. M., Darbeheshti, M.,
791 Baumgardner, D. G., and Kok, G. L.: Single-particle measurements of midlatitude black carbon and light-scattering
792 aerosols from the boundary layer to the lower stratosphere, *Journal of Geophysical Research: Atmospheres*, 111, 2006.

793 Seinfeld, J. H. and Pandis, S. N.: *Atmospheric Chemistry and Physics, Third.*, John Wiley, New York, 2016.

794 Shah, V., Jacob, D. J., Moch, J. M., Wang, X., and Zhai, S.: Global modeling of cloud water acidity, precipitation
795 acidity, and acid inputs to ecosystems, *Atmos Chem Phys*, 20, 12223–12245, [https://doi.org/10.5194/acp-20-12223-](https://doi.org/10.5194/acp-20-12223-2020)
796 2020, 2020.

797 Snider, G., Weagle, C. L., Murdymootoo, K. K., Ring, A., Ritchie, Y., Stone, E., Walsh, A., Akoshile, C., Anh, N. X.,
798 Balasubramanian, R., Brook, J., Qonitan, F. D., Dong, J., Griffith, D., He, K., Holben, B. N., Kahn, R., Lagrosas, N.,
799 Lestari, P., Ma, Z., Misra, A., Norford, L. K., Quel, E. J., Salam, A., Schichtel, B., Segev, L., Tripathi, S., Wang, C.,
800 Yu, C., Zhang, Q., Zhang, Y., Brauer, M., Cohen, A., Gibson, M. D., Liu, Y., Martins, J. V., Rudich, Y., and Martin,
801 R. V.: Variation in global chemical composition of PM_{2.5}: emerging results from SPARTAN, *Atmos Chem Phys*, 16,
802 9629–9653, <https://doi.org/10.5194/acp-16-9629-2016>, 2016.

803 Sullivan, A. P., Guo, H., Schroder, J. C., Campuzano-Jost, P., Jimenez, J. L., Campos, T., Shah, V., Jaeglé, L., Lee,
804 B. H., Lopez-Hilfiker, F. D., Thornton, J. A., Brown, S. S., and Weber, R. J.: Biomass Burning Markers and

805 Residential Burning in the WINTER Aircraft Campaign, *Journal of Geophysical Research: Atmospheres*, 124, 1846–
806 1861, <https://doi.org/10.1029/2017JD028153>, 2019.

807 Sun, J., Zhang, Q., Canagaratna, M. R., Zhang, Y., Ng, N. L., Sun, Y., Jayne, J. T., Zhang, X., Zhang, X., and Worsnop,
808 D. R.: Corrigendum to “Highly time- and size-resolved characterization of submicron aerosol particles in Beijing
809 using an Aerodyne Aerosol Mass Spectrometer” [*Atmos. Environ.* 44 (2010) 131-140], *Atmos Environ*, 47, 570,
810 <https://doi.org/10.1016/j.atmosenv.2010.01.023>, 2012.

811 Sun, Y. L., Zhang, Q., Schwab, J. J., Chen, W. N., Bae, M. S., Lin, Y. C., Hung, H. M., and Demerjian, K. L.: A case
812 study of aerosol processing and evolution in summer in New York City, *Atmos Chem Phys*, 11, 12737–12750,
813 <https://doi.org/10.5194/acp-11-12737-2011>, 2011.

814 Szopa, S., Balkanski, Y., Schulz, M., Bekki, S., Cugnet, D., Fortems-Cheiney, A., Turquety, S., Cozic, A., Déandreis,
815 C., Hauglustaine, D., Idelkadi, A., Lathièrè, J., Lefevre, F., Marchand, M., Vuolo, R., Yan, N., and Dufresne, J. L.:
816 Aerosol and ozone changes as forcing for climate evolution between 1850 and 2100, *Clim Dyn*, 40, 2223–2250,
817 <https://doi.org/10.1007/s00382-012-1408-y>, 2013.

818 Tian, P., Liu, D., Huang, M., Liu, Q., Zhao, D., Ran, L., Deng, Z., Wu, Y., Fu, S., Bi, K., Gao, Q., He, H., Xue, H.,
819 and Ding, D.: The evolution of an aerosol event observed from aircraft in Beijing: An insight into regional pollution
820 transport, *Atmos Environ*, 206, 11–20, <https://doi.org/10.1016/j.atmosenv.2019.02.005>, 2019.

821 Timonen, H., Aurela, M., Carbone, S., Saarnio, K., Saarikoski, S., Mäkelä, T., Kulmala, M., Kerminen, V.-M.,
822 Worsnop, D. R., and Hillamo, R.: High time-resolution chemical characterization of the water-soluble fraction of
823 ambient aerosols with PILS-TOC-IC and AMS, *Atmos Meas Tech*, 3, 1063–1074, 2010.

824 Twomey, S.: Pollution and the Planetary Albedo, *Atmos Environ*, 41, 120–125,
825 <https://doi.org/10.1016/j.atmosenv.2007.10.062>, 2007.

826 Wang, J., Xu, X., Ding, S., Zeng, J., Spurr, R., Liu, X., Chance, K., and Mishchenko, M.: A numerical testbed for
827 remote sensing of aerosols, and its demonstration for evaluating retrieval synergy from a geostationary satellite
828 constellation of GEO-CAPE and GOES-R, *J Quant Spectrosc Radiat Transf*, 146, 510–528,
829 <https://doi.org/10.1016/j.jqsrt.2014.03.020>, 2014a.

830 Wang, Q., Jacob, D. J., Spackman, J. R., Perring, A. E., Schwarz, J. P., Moteki, N., Marais, E. A., Ge, C., Wang, J.,
831 and Barrett, S. R. H.: Global budget and radiative forcing of black carbon aerosol: Constraints from pole-to-pole
832 (HIPPO) observations across the Pacific, *J Geophys Res*, 119, 195–206, <https://doi.org/10.1002/2013JD020824>,
833 2014b.

834 Wang, Y., Jacob, D. J., and Logan, J. A.: Global simulation of tropospheric O₃-NO_x-hydrocarbon chemistry - 1.
835 Model formulation, *Journal of Geophysical Research: Atmospheres*, 103, 10713–10725,
836 <https://doi.org/10.1029/98jd00158>, 1998.

837 Weagle, C. L., Snider, G., Li, C., Van Donkelaar, A., Philip, S., Bissonnette, P., Burke, J., Jackson, J., Latimer, R.,
838 Stone, E., Abboud, I., Akoshile, C., Anh, N. X., Brook, J. R., Cohen, A., Dong, J., Gibson, M. D., Griffith, D., He, K.

839 B., Holben, B. N., Kahn, R., Keller, C. A., Kim, J. S., Lagrosas, N., Lestari, P., Khian, Y. L., Liu, Y., Marais, E. A.,
840 Martins, J. V., Misra, A., Muliane, U., Pratiwi, R., Quel, E. J., Salam, A., Segev, L., Tripathi, S. N., Wang, C., Zhang,
841 Q., Brauer, M., Rudich, Y., and Martin, R. V.: Global Sources of Fine Particulate Matter: Interpretation of PM_{2.5}
842 Chemical Composition Observed by SPARTAN using a Global Chemical Transport Model, *Environ Sci Technol*, 52,
843 11670–11681, <https://doi.org/10.1021/acs.est.8b01658>, 2018.

844 Weinheimer, A. J., Walega, J. G., Ridley, B. A., Sachse, G. W., Anderson, B. E., and Collins Jr, J. E.: Stratospheric
845 NO_y measurements on the NASA DC-8 during AASE II, *Geophys Res Lett*, 20, 2563–2566, 1993.

846 Weng, H., Lin, J., Martin, R., Millet, D. B., Jaeglé, L., Ridley, D., Keller, C., Li, C., Du, M., and Meng, J.: Global
847 high-resolution emissions of soil NO_x, sea salt aerosols, and biogenic volatile organic compounds, *Sci Data*, 7, 1–15,
848 <https://doi.org/10.1038/s41597-020-0488-5>, 2020.

849 Van Der Werf, G. R., Randerson, J. T., Giglio, L., Van Leeuwen, T. T., Chen, Y., Rogers, B. M., Mu, M., Van Marle,
850 M. J. E., Morton, D. C., Collatz, G. J., Yokelson, R. J., and Kasibhatla, P. S.: Global fire emissions estimates during
851 1997–2016, *Earth Syst Sci Data*, 9, 697–720, <https://doi.org/10.5194/essd-9-697-2017>, 2017.

852 Westervelt, D. M., Pierce, J. R., Riipinen, I., Trivitayanurak, W., Hamed, A., Kulmala, M., Laaksonen, A., Decesari,
853 S., and Adams, P. J.: Formation and growth of nucleated particles into cloud condensation nuclei: Model-measurement
854 comparison, *Atmos Chem Phys*, 13, 7645–7663, <https://doi.org/10.5194/acp-13-7645-2013>, 2013.

855 Whitey, K. T.: The physical characteristics of sulfur aerosols, in: *Atmospheric Environment*, vol. 41, Elsevier, 25–49,
856 <https://doi.org/10.1016/j.atmosenv.2007.10.057>, 1978.

857 Yu, F. and Luo, G.: Simulation of particle size distribution with a global aerosol model: Contribution of nucleation to
858 aerosol and CCN number concentrations, *Atmos Chem Phys*, 9, 7691–7710, <https://doi.org/10.5194/acp-9-7691-2009>,
859 2009.

860 Yue, D. L., Hu, M., Wu, Z. J., Guo, S., Wen, M. T., Nowak, A., Wehner, B., Wiedensohler, A., Takegawa, N., and
861 Kondo, Y.: Variation of particle number size distributions and chemical compositions at the urban and downwind
862 regional sites in the Pearl River Delta during summertime pollution episodes, *Atmos Chem Phys*, 10, 9431–9439,
863 2010.

864 Zender, C. S., Bian, H., and Newman, D.: Mineral Dust Entrainment and Deposition (DEAD) model: Description and
865 1990s dust climatology, *Journal of Geophysical Research: Atmospheres*, 108, <https://doi.org/10.1029/2002jd002775>,
866 2003.

867 Zhai, S., Jacob, D., Brewer, J., Li, K., Moch, J., Kim, J., Lee, S., Lim, H., Lee, H. C., Kuk, S. K., Park, R., Jeong, J.,
868 Wang, X., Liu, P., Luo, G., Yu, F., Meng, J., Martin, R., Travis, K., Hair, J., Anderson, B., Dibb, J., Jimenez, J.,
869 Campuzano-Jost, P., Nault, B., Woo, J.-H., Kim, Y., Zhang, Q., and Liao, H.: Interpretation of geostationary satellite
870 aerosol optical depth (AOD) over East Asia in relation to fine particulate matter (PM_{2.5}): insights from the KORUS-
871 AQ aircraft campaign and seasonality, *Atmos Chem Phys*, 1–23, <https://doi.org/10.5194/acp-2021-413>, 2021.

872 Zhang, L., Kok, J. F., Henze, D. K., Li, Q., and Zhao, C.: Improving simulations of fine dust surface concentrations
873 over the western United States by optimizing the particle size distribution, *Geophys Res Lett*, 40, 3270–3275,
874 <https://doi.org/10.1002/grl.50591>, 2013.

875